Influence of a Subtype of Inhibitory Interneuron on Stimulus-Specific Responses in Visual Cortex

Rong Mao[1,2], James Schummers[1,2], Ulf Knoblich[2,3], Carolyn J. Lacey[4], Audra Van Wart[1,2], Inma Cobos[5], Carol Kim[5], John R. Huguenard[4], John L. R. Rubenstein[5] and Mriganka Sur[1,2]

[1]Picower Institute for Learning and Memory, Cambridge, MA 02139, USA, [2]Department of Brain and Cognitive Sciences, Massachusetts Institute of Technology, Cambridge, MA 02139, USA, [3]McGovern Institute for Brain Research, Cambridge, MA 02139, USA, [4]Department of Neurology and Neurological Sciences, Stanford University School of Medicine, Stanford, CA 94305, USA and [5]Nina Ireland Laboratory of Developmental Neurobiology, Center for Neurobiology and Psychiatry, Department of Psychiatry, University of California, San Francisco, CA 94158, USA

Address correspondence to Rong Mao, Picower Institute for Learning and Memory and Department of Brain and Cognitive Sciences, Massachusetts Institute of Technology, 77 Massachusetts Avenue, 46-6237, Cambridge, MA 02139, USA. Email: rmao@stanford.edu.

Inhibition modulates receptive field properties and integrative responses of neurons in cortical circuits. The contribution of specific interneuron classes to cortical circuits and emergent responses is unknown. Here, we examined neuronal responses in primary visual cortex (V1) of adult $Dlx1^{-/-}$ mice, which have a selective reduction in cortical dendrite-targeting interneurons (DTIs) that express calretinin, neuropeptide Y, and somatostatin. The V1 neurons examined in $Dlx1^{-/-}$ mice have reduced orientation selectivity and altered firing rates, with elevated late responses, suggesting that local inhibition at dendrites has a specific role in modulating neuronal computations. We did not detect overt changes in the physiological properties of thalamic relay neurons and features of thalamocortical projections, such as retinotopic maps and eye-specific inputs, in the mutant mice, suggesting that the defects are cortical in origin. These experimental results are well explained by a computational model that integrates broad tuning from dendrite-targeting and narrower tuning from soma-targeting interneuron subclasses. Our findings suggest a key role for DTIs in the fine-tuning of stimulus-specific cortical responses.

Keywords: cortex, dendrite, inhibition, orientation, tuning

Introduction

γ-Aminobutyric acid (GABA)ergic inhibitory interneurons are integral to cortical development and function. While these cells comprise merely 20–30% of neocortical neurons, they exhibit the greatest diversity in morphological, physiological, molecular, and synaptic characteristics (DeFelipe 1993; Markram et al. 2004; Blatow et al. 2005; Ascoli et al. 2008). Among different classes of interneurons, basket cells project to soma and proximal dendrites of excitatory neurons, chandelier cells innervate initial axon segment, whereas double bouquet, bipolar, bitufted, and Martinotti cells target dendrites and dendritic tufts (DeFelipe 1993; Markram et al. 2004). Furthermore, chandelier and typical basket cells express parvalbumin and are fast spiking; other basket cells express cholecystokinin (CCK) and/or vasoactive intestinal peptide (VIP), are adapting/regular spiking or irregular spiking, and fire action potentials with frequency adaptation (Kawaguchi and Kubota 1997, 1998; Kubota and Kawaguchi 1997; Wang et al. 2002; Galarreta et al. 2004); small basket cells express VIP and are regular spiking (Kawaguchi and Kubota 1997; Wang et al. 2002); dendrite- and tuft-targeting interneurons express somatostatin, neuropeptide Y (NPY), and calretinin and are accommodating (regular spiking) or for a small fraction irregular spiking (DeFelipe 1993; Chow et al. 1999; Markram et al. 2004; Toledo-Rodriguez et al. 2004; Xu et al. 2006; Gonchar et al. 2007).

Most GABAergic interneurons in the rodent neocortex derive from subpallial progenitors in the caudal or medial ganglionic eminences (CGE and MGE) (Marin and Rubenstein 2001; Wonders and Anderson 2006): parvalbumin+ and somatostatin+ interneurons originate in the MGE, while many calretinin+ and NPY+ interneurons are generated in the CGE (Xu et al. 2004; Butt et al. 2005). Several genes that encode homeobox transcription factors are critical for development of interneurons, including $Nkx2.1$ (Sussel et al. 1999; Butt et al. 2008), $Lhx6$ (Liodis et al. 2007; Zhao et al. 2008), and $Dlx1$ and $Dlx2$ (Anderson et al. 1997; Cobos et al. 2007). In particular, $Dlx1$ is required for survival of somatostatin+, NPY+, and calretinin+ interneurons—mice that lack $Dlx1$ show a selective reduction in these dendrite-innervating cortical interneurons (Cobos et al. 2005).

Given their diverse properties, different classes of interneurons likely have distinct roles in modulating integrative responses and receptive field properties of excitatory neurons. For example, GABAergic basket cells influence ocular dominance plasticity in visual cortex (Fagiolini et al. 2004; Yazaki-Sugiyama et al. 2009). Furthermore, parvalbumin+ interneurons are critical for generating gamma oscillations that may be important for cortical information processing (Cardin et al. 2009; Sohal et al. 2009). Inhibitory mechanisms involving distinct roles of interneuron subtypes may also underlie receptive field properties in visual cortex. A paradigmatic emergent property created by circuitry in the primary visual cortex (V1) is orientation selectivity (Somers et al. 1995; Ferster and Miller 2000). The role of inhibition in creating orientation selectivity is unresolved, with some studies claiming a critical role for intracortical inhibition in sharpening orientation tuning (Sillito 1975; Eysel et al. 1998), others indicating that thalamocortical excitation provides sufficient selectivity and inhibition has little role (Nelson et al. 1994; Ferster et al. 1996; Chung and Ferster 1998; Finn et al. 2007; Priebe and Ferster 2008), and still others arguing for a combination of thalamocortical plus intracortical excitation together with intracortical inhibition in shaping selectivity (Somers et al. 1995; Vidyasagar et al. 1996; Schummers et al. 2002; Shapley et al. 2003; Marino et al. 2005). Thus, we reasoned that it would be timely and instructive to examine whether the loss of dendrite-innervating interneurons results

in systematic alterations in orientation selectivity and other response properties of V1 neurons.

We have measured the effects of selectively reducing dendrite-innervating interneurons on stimulus-specific V1 responses in $Dlx1^{-/-}$ mice (Cobos et al. 2005)—due to their selective reduction of dendrite-innervating interneurons, these mice provide an opportunity to measure the effects of selectively reducing this subtype of interneuron on stimulus-specific V1 responses. We report that orientation tuned responses are broadened and firing rates are altered in $Dlx1^{-/-}$ mice, while other aspects of V1 physiology and thalamic inhibitory circuits appear normal. A computational model that captures our experimental findings indicates that different interneuron subclasses with specific response tuning can contribute to the generation of feature-selective responses in cortical circuits.

Materials and Methods

Animals
Mutant $Dlx1^{-/-}$ mice (Qiu et al. 1997) were maintained on a C57BL/6J × CD1 mixed genetic background to increase their viability (Cobos et al. 2005). Wild-type littermates were used as controls. Mouse colonies were maintained at the Massachusetts Institute of Technology (MIT), the University of California, San Francisco (UCSF), and Stanford University in accordance with guidelines of the National Institutes of Health, MIT, UCSF, and Stanford, and all experiments were performed with approval from Institutional Animal Care and Use Committees. $Dlx1^{-/-}$ mice and their wild-type littermates at ages of ≥postnatal days 60 were used in all experiments except in vitro slice recording.

Because $Dlx1^{-/-}$ mice show handle-induced seizures (Cobos et al. 2005), we attempted to avoid such seizure incidences by habituating the animals for 3–5 sessions (~10 min in each session, once a day) prior to the day of experiments. In these habituation sessions, mice were acclimated to the room and handling of the experimenter. The experimenter wore gloves, socialized with the mice, allowing them to walk or run from hand to hand, until the mice showed no apparent signs of stress or fear. We did not observe any seizure activity in $Dlx1$ mutant animals during the handling. These procedures helped minimize occurrence of seizures in the mutant mice: Very few mice displayed seizure episodes, as assessed by a 5-stage scale (Racine 1972), during the experiments described below. Mice that exhibited seizures were excluded from data analysis.

Histology and Cell Counting
Adult mice (~2 months old) were deeply anesthetized with Avertin (Sigma; 0.2 mL/10 g body weight) and perfused intracardially with 4% paraformaldehyde in phosphate-buffered saline (PBS) solution (pH 7.4). The brains were removed, cut through the sagittal midline, postfixed overnight in the same fixative, and cryoprotected by immersion in 30% sucrose/PBS. Coronal sections of one hemisphere were cut at a thickness of 40 μm on a sliding microtome. Free-floating immunohistochemistry using polyclonal antibodies against parvalbumin (rabbit, 1:1000; Chemicon), calretinin (rabbit, 1:4000; Swant Swiss Abs or 1:500; Chemicon), somatostatin (rat, 1:500; Chemicon), NPY (rabbit, 1:4000; Immunostar), and Neuronal Nuclei (NeuN; mouse, 1:500; Chemicon) was performed. The other hemisphere was embedded in TBS medium (Triangle Biomedical Science). Coronal sections at a thickness of 10 μm were cut on a cryostat and mounted on Fisher Superfrost/Plus slides. mRNA in situ hybridization using digoxigenin-labeled probes against $Gad67$ and $somatostatin$ (the sources of these probes were Brian Condie and Tom Lufkin, respectively) were performed according to previously established methods (Palop et al. 2010). For both immunohistochemistry and in situ hybridization, Nissl staining on adjacent sections was performed to aid in identifying the laminar distributions of the different neuronal subtypes as well as the reticular nucleus (nRT) and dorsal lateral geniculate nucleus (dLGN) of the thalamus.

Experiments were performed in parallel for $Dlx1^{+/+}$ and $Dlx1^{-/-}$ littermate mice, on at least 3–4 mice per genotype. Each experiment was repeated at least twice.

Nonstereological count methods were used to compare the number of neuronal bodies stained by immunohistochemistry or RNA in situ hybridization in mutant and control mice. The experimenter was blinded to genotype in all histological procedures, including sampling, data collection, and statistic analysis. Counts were performed on digitized images acquired using a Nikon Eclipse 80i microscope and Nikon Elements Software, at a magnification of 10×. Cell counting was performed on 2–3 coronal sections per animal in layers 2–3, 4, 5, and 6 of visual cortex, as well as in the nRT and dLGN. In all cases, samples from similar rostrocaudal levels in mutant and controls were selected. For quantifications in visual cortex, coronal sections were selected using stereotaxic coordinates between bregma levels –2.92 and –4.20 mm (Paxinos and Franklin 2001). A 1-mm strip of cortex from the white matter to the pial surface was analyzed in each section (1.2 mm² each). Values from the 2 trials performed on the same animal were averaged. The values from each mutant were normalized to their wild-type littermate controls. Percentage of change is presented as mean ±standard error of the mean (SEM). Statistical analysis was performed using the Student's t-test (2-tailed unequal variance, $\alpha = 0.05$) with Bonferroni corrections to calculate P values.

In vitro Slice Preparation
Brain slices were prepared from $Dlx^{+/+}$ and $Dlx1^{-/-}$ mice (2–3 weeks and 1–2 months). Briefly, the mice were anesthetized with pentobarbital (50 mg/kg), decapitated, and the brains rapidly removed and immersed in an ice-cold (4 °C) slicing solution containing (in mM): 234 sucrose, 2.5 KCl, 1.25 NaH₂PO₄, 10 MgSO₄, 0.5 CaCl₂, 26 NaHCO₃, and 11 glucose; equilibrated with 95% O₂ and 5% CO₂; pH 7.4. In the majority of older mice, the mice were first quickly perfused transcardially with 50 mL of the ice-cold slicing solution prior to decapitation. Horizontal thalamic slices (260 μm) containing the nRT and dLGN were cut and incubated in artificial cerebrospinal fluid containing (in mM): 126 NaCl, 2.5 KCl, 1.25 NaH₂PO₄, 1 MgCl₂, 2 CaCl₂, 26 NaHCO₃, and 10 glucose; equilibrated with 95% O₂ and 5% CO₂; pH 7.4, initially at 32 °C for 1 h, and subsequently at room temperature, before being transferred to a recording chamber.

In vitro Patch Clamp Recordings
Thalamic neurons from nRT or dLGN were visually identified using infrared video microscopy. In addition, the identity of the cells was confirmed based on electrophysiological criteria related to the action potential firing of nRt cells and T-type current response of dLGN cells. Recordings were performed at room temperature in whole-cell configuration. Electrodes (tip resistance of 2–4 MΩ) were filled with internal solution containing (in mM): 120 K-gluconate, 11 KCl, 1 CaCl₂, 1 MgCl₂, 10 4-(2-hydroxyethyl)-1-piperazineethanesulfonic acid (HEPES), 1 ethyleneglycol-bis(2-aminoethylether)-N,N,N',N'-tetra acetic acid (EGTA) pH 7.3 adjusted with KOH, 290 mOsm for excitatory postsynaptic current (EPSC) recordings or 135 CsCl, 10 HEPES, 10 EGTA, 2 MgCl₂, 5 QX-314 pH 7.3 adjusted with CsOH, 300 mOSm for inhibitory postsynaptic current (IPSC) recordings. For EPSC recordings, EPSCs were isolated in 50 μM picrotoxin (Tocris), a GABA$_A$ receptor blocker, and for IPSC recordings, IPSCs were isolated in 20 μM 6,7-dinitroquinoxaline-2,3-dione (DNQX), an amino-3-hydroxy-5-methyl-4-isoxazolepropionic acid (AMPA) and kainite receptor antagonist and 50 μM D-(-)-2-amino-5-phosphonopentanoic acid (D-AP5), a N-methyl-D-aspartic acid (NMDA) receptor antagonist (Ascent Scientific), all by bath application. The access resistance was always <18 MΩ and constantly monitored for stability.

In vitro Data Acquisition and Analysis
Signals were amplified with a Multiclamp 700A amplifier (Axon Instruments), low-pass filtered at 20 KHz and sampled at 4 or 10 kHz. A Digidata 1320 digitizer (Axon Instruments) and pClamp9 (Axon Instruments) were used for data acquisition. Locally written software (J. R. Huguenard, Stanford University School of Medicine) was used to detect (Wdetecta, a program to detect postsynaptic current), sort, and

isolate (winscanselect, a program to select events above noise level) spontaneous EPSCs (sEPSCs) and spontaneous IPSCs (sIPSCs). Data were then analyzed with Clampfit 9 (Axon instruments) and Origin (Microcal Software). The frequency, amplitude, half-width, rise, and decay times of sEPSCs and sIPSCs were used for quantification. Results are presented as mean $\pm$ SEM. Data obtained were statistically compared by using Mann–Whitney tests (2-tailed). Differences were considered significant if $P < 0.05$.

Optical Imaging of Intrinsic Signals

Mice were anesthetized using urethane (1.0 g/kg, intraperitoneally [i.p.]) and chlorprothixene (0.2 mg, i.p.), supplemented as necessary throughout imaging. During the experiment, the animal's physiological condition was continuously monitored: temperature was maintained at 37–38 °C with a homeothermic heating blanket, the eyes were periodically lubricated with silicone oil, and the animal was continuously oxygenated. The skull was exposed and a custom-made plate was glued on the head to minimize movement. The skull was thinned over V1 (in the same hemisphere across all animals) with a dremel drill and covered with an agarose solution (1.5%) and a glass coverslip. The cortical surface was illuminated with red light (630 nm), and intrinsic signals were imaged with a charge-coupled device camera (Cascade 512B, Roper Scientific).

Intrinsic signal maps from a region of visual space (72° × 72°) were acquired during periodic stimulation (9 s/cycle) with a drifting horizontal or vertical white bar (9° × 72°) over a uniformly gray background, randomly presented to either eye (monocularly) or to both eyes simultaneously. Images of visual cortex were captured at 15 frames/s during each stimulus session of 25 min. A temporal high pass filter (135 frames) was used to remove slow noise components, after which the temporal Fast Fourier Transform (FFT) component at the stimulus frequency was calculated, pixel by pixel, from the whole set of images. The strength of visually driven responses for each eye was measured from the amplitude of the FFT component, and maps of relative retinotopy were computed from the phase of the response. Ocular dominance index (ODI) was calculated from each eye's response (R) at each pixel as ODI = ($R_{contra} - R_{ipsi}$)/ ($R_{contra} + R_{ipsi}$), and ODI values from within the binocular zone were averaged for comparison across animals. The binocular zone was defined as the region with ipsilateral eye drive as well as contralateral drive. All pixels that had magnitude above 60% of the maximum level were considered responsive and thus included for analysis. To assess retinotopic map quality between wild-type and $Dlx1^{-/-}$ mice, a region of 50 × 50 pixels (900 µm²) was selected at a similar retinotopic location within the elevation map for each mouse. Scatter was then calculated as the difference in retinotopy between each pixel and the mean of the surrounding 25 pixels. Differences between wild-type and $Dlx1^{-/-}$ mice were compared using Student's t-tests (2-sided unequal variance, based on normal distributions of the data and heterogeneous variance across groups), with the following exception: the P value for comparison of scatter between V1 and background from nonvisual cortical regions (see Fig. 1 legend) was calculated by a Wilcoxon rank sum test (2-sided, based on absence of normal distributions).

In Vivo Electrophysiology

Single units were recorded with tungsten microelectrodes (2–4 MΩ resistance, FHC) as described (Dragoi et al. 2000). Briefly, mice were given atropine (0.54 µg/g) to decrease bronchial and salivary secretions and then anesthetized with Nembutal (pentobarbital, 0.05 mg/g), supplemented as necessary throughout recording. The body temperature of the animal was monitored by a rectal probe and maintained at 37–38 °C by a homeothermic heating pad. The animal's eyes were covered with ophthalmic ointment until recording began, at which time the ointment was carefully wiped off and a thin layer of silicone oil was applied to the eyes. A metal plate was glued to the head of the animal; this plate was attached to a holder to maintain stability during the craniotomy and recording sessions. A dental drill and sharp forceps were used to perform a craniotomy to expose V1; the brain was covered with 2% agar.
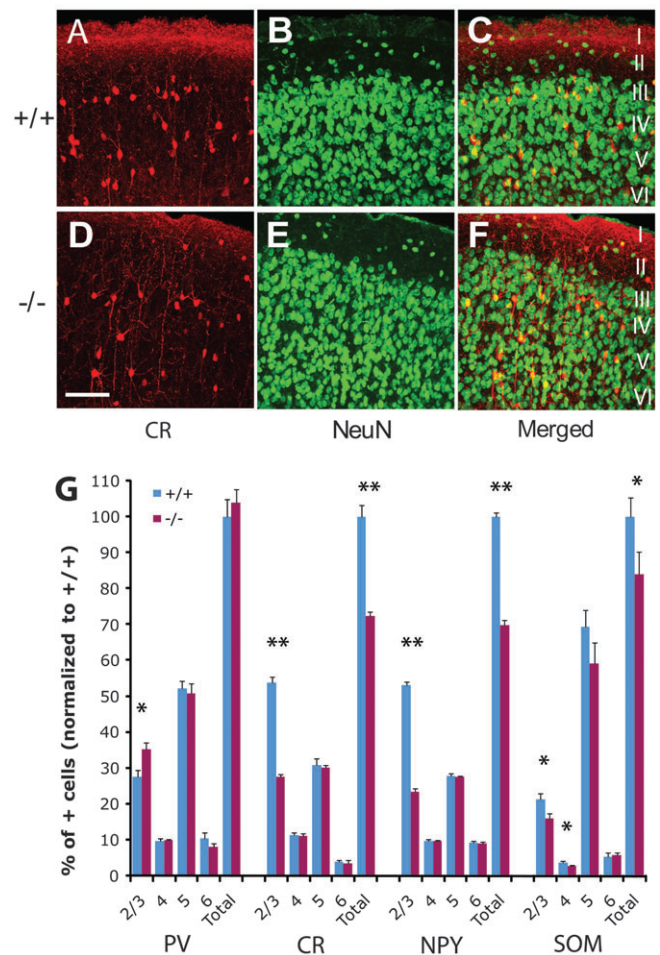

Figure 1. Adult $Dlx1^{-/-}$ mice showed a partial reduction in calretinin+, NPY+, and somatostatin+ neurons in visual cortex. (A–F) Examples of representative calretinin+ and NeuN+ cells, and the merged images, as shown by immunohistochemistry in wild-type (A–C) and $Dlx1^{-/-}$ littermates (D–F). Scale bar: 100 µm (A–F). The variation in density of calretinin staining in layer 1 is potentially due to differences in background staining/edge effects, and/or staining of neuronal processes. (G) The percents of parvalbumin+, calretinin+, NPY+, and somatostatin+ cells in each laminar layer (layers 2/3, 4, 5, and 6), normalized to that of the total number of positive neurons in $Dlx1^{+/+}$ littermates, were quantified in visual cortices of $Dlx1^{-/-}$ ($n = 4$) and $Dlx1^{+/+}$ mice ($n = 3$). PV: parvalbumin+; CR: calretinin+; NPY: NPY+; SOM: somatostatin+. For all comparisons, $*P < 0.05$; $**P < 0.01$.

Units were isolated from all layers of V1 (DataWave Technologies or Plexon Neurotechnology Research Systems). A computer monitor, placed at 30 cm from the animal, was used to present visual stimuli. For orientation tuning measurements, the stimuli consisted of full-field 16 high-contrast square wave gratings at varying orientations, differing by 22.5° intervals (spatial frequency of 0.05 cycle/degree, temporal frequency of 4 Hz, 100% contrast). During each trial, all 16 gratings and a blank screen of uniform intermediate gray were randomly interleaved; each was presented for 2 s, with 500 ms intervals between each stimulus. Data from 20 to 30 trials were recorded for each cell.

Analysis of Orientation Selectivity

Cluster sorting was performed using DataWave or Plexon software. Peristimulus time histograms (PSTHs) were constructed with 10-ms bins and averaged across all 16 conditions with visual stimuli at different orientations. Units were classified as visually responsive if their instantaneous firing rates (binned over 10-ms intervals) during the first 150 ms after stimulus onset were at least 4 standard deviations above the mean of prestimulus spontaneous firing rates (measured over 350 ms). Cells selected for detailed analysis had ⩾1 Hz average evoked firing rates

during the late response (defined below) at the preferred direction. Firing rate responses to each orientation, either maximal instantaneous at the initial transient peaks (10 ms average) or averaged over 250 ms of the late "steady-state" responses, were averaged from all trials, and the spontaneous firing rates were subtracted. Tuning curves based on these transient or late responses were generated by aligning the preferred direction of each cell to 90° and averaging these aligned responses. Orientation selectivity index (OSI) was calculated using a vector averaging method, and the preferred orientation was determined from the angle of the mean orientation vector (Swindale 1998; Dragoi et al. 2000). Values for OSIs, firing rates, and ratios (and also those from modeling in the following section) are presented as mean $\pm$ SEM. All P values were calculated using Wilcoxon rank sum tests (2-sided, $\alpha = 0.05$) except for the following: P values for comparisons of individual data points (binned over 10 ms) on the PSTHs and for comparisons of tuning curves were calculated using 2-way analysis of variance (with genotypes and stimulus conditions as the 2 factors; $\alpha = 0.05$).

Computational Model

We constructed a simplified cortical network model which was organized in a feed-forward sequence of 5 2-dimensional layers of cells. Within each layer, the preferred orientation of the cells varied along the first dimension between 0° and 180° and was constant along the second dimension.

There were 2 input layers and 3 processing layers representing 3 different types of cortical neurons. The first input layer provided stimulus-independent "background" (B) activity while the second layer represented stimulus-dependent inputs (I). Each input layer consisted of 512 cells. The 3 processing layers consisted of excitatory pyramidal cells, soma-targeting interneurons (STIs), and dendrite-targeting interneurons (DTIs), respectively. STIs were modeled as parvalbumin+, fast-spiking basket cells, while DTI's properties were consistent with somatostatin+, NPY+, and/or calretinin+, regular-spiking cells. The time constants for DTIs and STIs were tuned to match the physiological properties of fast-spiking versus regular-spiking GABAergic neurons. There were a total of 684 cells including 512 pyramidal cells (75% of total cells), 112 STI cells (15%), and 60 DTI cells (10%), matching the cortical proportions of these different cell types (Markram et al. 2004). Both B and I input layers provided excitatory inputs to all 3 processing layers. Both STI and DTI layers provided inhibition to pyramidal cells. Synaptic connections between layers were made such that each postsynaptic cell received input from presynaptic cells with similar orientation preferences.

Cell Parameters

Input (B and I) cells were modeled as independent variable rate Poisson process spike generators with a time step of 100 μs. Pyramidal (P) cells had a single somatic compartment with 6 dendritic compartments attached. The somatic compartment was based on the single compartment Hodgkin–Huxley type model (Golomb and Amitai 1997), and adapted to include additional dendritic compartments. The membrane potential was determined by the membrane equation summing currents from different intrinsic currents through channels present in the membrane with synaptic and injected currents.

For the soma:

$$C_m \frac{\mathrm{d}V_m}{\mathrm{d}t} = I_L + I_{Na} + I_{NaP} + I_{KDr} + I_{Ka} + I_{Ks} + I_{syn} + I_{inj}$$

$C_m = 1.5 \ \mu F/cm^2$.

Leak current:

$$I_L = g_L(E_L - V_m)$$

$g_L = 0.20 \ mS/cm^2$, $E_L = -65 \ mV$.

Fast sodium channels:

$$I_{Na} = g_{Na}(E_{Na} - V_m)m^3 b$$

$$m = m_\infty = \frac{1}{1 + e^{-\frac{V_m - \theta_m}{\sigma_m}}}$$

$$b_\infty = \frac{1}{1 + e^{-\frac{V_m - \theta_b}{\sigma_b}}}$$

$$\tau_b = 0.37 + \frac{2.78}{1 + e^{-\frac{V_m - \theta_{bt}}{\sigma_{bt}}}}$$

$$\frac{\mathrm{d}b}{\mathrm{d}t} = \frac{b_\infty - b}{\tau_b}$$

$g_{Na} = 48.0 \ mS/cm^2$, $E_{Na} = 55 \ mV$, $\theta_m = -30.0 \ mV$, $\sigma_m = 9.5 \ mV$, $\theta_b = -53.0 \ mV$, $\sigma_b = -7.0 \ mV$, $\theta_{bt} = -40.5 \ mV$, $\sigma_{bt} = -6.0 \ mV$.

Persistent sodium channels:

$$I_{NaP} = g_{NaP}(E_{Na} - V_m)p$$

$$p = p_\infty = \frac{1}{1 + e^{-\frac{V_m - \theta_p}{\sigma_p}}},$$

$g_{NaP} = 0.14 \ mS/cm^2$, $E_{Na} = 55 \ mV$, $\theta_p = -40.0 \ mV$, $\sigma_m = 5.0 \ mV$.

Delayed rectifier potassium channels:

$$I_{KDr} = g_{KDr}(E_K - V_m)n^4$$

$$n_\infty = \frac{1}{1 + e^{-\frac{V_m - \theta_n}{\sigma_n}}}$$

$$\tau_n = 0.37 + \frac{1.85}{1 + e^{-\frac{V_m - \theta_{nt}}{\sigma_{nt}}}}$$

$$\frac{\mathrm{d}n}{\mathrm{d}t} = \frac{n_\infty - n}{\tau_n}$$

$g_{KDr} = 6.0 \ mS/cm^2$, $E_K = -90 \ mV$, $\theta_n = -30.0 \ mV$, $\sigma_n = 10.0 \ mV$, $\theta_{nt} = -27.0 \ mV$, $\sigma_{nt} = -15.0 \ mV$.

A-type potassium channels:

$$I_{Ka} = g_{Ka}(E_K - V_m)a^3 b$$

$$a = a_\infty = \frac{1}{1 + e^{-\frac{V_m - \theta_a}{\sigma_a}}}$$

$$b_\infty = \frac{1}{1 + e^{-\frac{V_m - \theta_b}{\sigma_b}}}$$

$$\frac{\mathrm{d}b}{\mathrm{d}t} = \frac{b_\infty - b}{\tau_b}$$

$g_{Ka} = 2.8 \ mS/cm^2$, $E_K = -90 \ mV$, $\theta_a = -50.0 \ mV$, $\sigma_a = 20.0 \ mV$, $\theta_b = -80.0 \ mV$, $\sigma_b = 6.0 \ mV$, $\tau_b = 15.0 \ ms$.

Slow potassium channels:

$$I_{Ks} = g_{Ks}(E_K - V_m)z$$

$$z_\infty = \frac{1}{1 + e^{-\frac{V_m - \theta_z}{\sigma_z}}}$$

$$\frac{\mathrm{d}z}{\mathrm{d}t} = \frac{z_\infty - z}{\tau_z}$$

$g_{Ks} = 0.80 \ mS/cm^2$, $E_K = -90 \ mV$, $\theta_z = -39.0 \ mV$, $\sigma_z = 5.0 \ mV$, $\tau_b = 75.0 \ ms$.

Synaptic currents:

$$I_{syn} = g_{syn}(E_{syn} - V_m)$$

$E_{AMPA} = 0 \ mV$, $E_{GABA_A} = -80 \ mV$, $E_{GABA_A} = -90 \ mV$.

The dendrites were modeled analogously but only contained passive (leak) channels.

DTIs (D) were modeled as single compartments. These neurons usually have regular-spiking characteristics similar to pyramidal neurons (Beierlein et al. 2003; Ma et al. 2006; Caputi et al. 2008) and were thus modeled using the same set of equations, adjusted for the lack of dendritic compartments. $g_L = 0.10 \ mS/cm^2$, $g_{Na} = 48.0 \ mS/cm^2$, $g_{NaP} = 0.14 \ mS/cm^2$, $g_{KDr} = 6.0 \ mS/cm^2$, $g_{Ka} = 2.8 \ mS/cm^2$, $g_{Ks} = 0.20 \ mS/cm^2$.

STIs (S) show very different properties including fast spikes, higher firing rates, lack of spike rate adaptation (Beierlein et al. 2003; Ma et al.

2006; Caputi et al. 2008) and were modeled as single compartments after the Hodgkin–Huxley type equations in a previous model (Wang and Buzsaki 1996):

$$C_m \frac{dV_m}{dt} = I_L + I_{Na} + I_{KDr} + I_{syn} + I_{inj}$$

C_m = 1.5 μF/cm^2.

Leak current:

$$I_L = g_L(E_L - V_m)$$

g_L = 0.40 mS/cm^2, E_L = −70 mV.

Fast sodium channels:

$$I_{Na} = g_{Na}(E_{Na} - V_m)m^3 h$$

$$\alpha_m = \frac{-0.1 \cdot (V_m + 35)}{e^{-0.1 \cdot (V_m + 35)} - 1}$$

$$\beta_z = 4e^{-\frac{V_m + 60}{18}}$$

$$m = m_\infty = \frac{\alpha_m}{\alpha_m + \beta_m}$$

$$\alpha_b = 0.07e^{-\frac{(V_m + 58)}{20}}$$

$$\beta_b = \frac{1}{e^{-0.1(V_m + 28)} + 1}$$

g_{Na} = 70.0 mS/cm^2, E_{Na} = 55 mV.

Delayed rectifier potassium channels:

$$I_{KDr} = g_{KDr}(E_K - V_m)n^4$$

$$\alpha_n = \frac{-0.1 \cdot (V_m + 34)}{e^{-0.1 \cdot (V_m + 34)} - 1}$$

$$\beta_n = 0.125e^{-\frac{V_m + 44}{80}}$$

$$m = m_\infty = \frac{\alpha_m}{\alpha_m + \beta_m}$$

g_{KDr} = 18.0 mS/cm^2, E_K = −90 mV.

Synaptic Dynamics

The model included 3 major synapse types, excitatory AMPA synapses and inhibitory GABA synapses including both GABA$_A$ and GABA$_B$ subtypes. All synapses were modeled by kinetic models with 2 states representing the open and closed states of ion channels (Destexhe et al. 1994). The fraction of open channels for a synapse r increases with the rate constant α when neurotransmitter is present (T = 1 mM) and decreases with the dissociation rate β:

$$\frac{dr}{dt} = \alpha T(1 - r) - \beta r$$

The total conductance g of a synapse was the product of its maximal conductance $\hat{g}$, the fraction of open channels r, and a factor that determined the depression state of the synapse D. Synaptic depression was modeled similar to the open channel fraction, adapted from a previous approach (Varela et al. 1997). In the nondepressed state, the full conductance of the synapse was available, represented by D = 1. Each time a synapse was active, its availability was decreased, governed by the rate constants α_D and β_D:

$$\frac{dD}{dt} = \alpha_D T(1 - D) - \beta_D D$$

The rate constants for the different synapse types (Destexhe et al. 1994) were: AMPA synapses: $\alpha = 1.1 \times 10^6$ M^{-1} s^{-1}, β = 190 s^{-1}; GABA$_A$: α = 0.53 × 10^6 M^{-1} s^{-1}, β = 180 s^{-1}; GABA$_B$: α = 16 × 10^6 M^{-1} s^{-1}, β = 4.7 s^{-1}. For depressing synapses: α_D = 0.1 × 10^3 M^{-1} s^{-1}, β_D = 4.0 s^{-1}; for nondepressing synapses: α_D = 0, β_D = 0.

Connectivity

Synaptic connections between layers were made such that each postsynaptic cell receives input from presynaptic cells with similar orientation preferences. The maximal distance between the orientation preferences of a pair of connected cells was determined by the input tuning. The standard input tuning for each connection in the model was 30°, that is, the maximal difference between the preferred orientation of the potential presynaptic cell and its postsynaptic target was 30°. Within this pool of potential presynaptic cells, the probability of an actual synaptic connection fell off with distance and was determined by a normal distribution with σ = 15°.

All excitatory synapses were modeled as AMPA/kainate synapses. STIs made GABA$_A$-ergic synapses onto the soma of pyramidal cells. DTIs made both GABA$_A$- and GABA$_B$-ergic synapses onto the dendrites of pyramidal cells. For each pair of connected layers, the total synaptic conductance was fixed as a parameter and the conductance of each individual synapse was computed by dividing the total conductance by the number of synapses for each postsynaptic neuron. The total conductances were: g_{BD} = 3.0 nS, g_{BS} = 70.0 nS, g_{BP} = 12.0 nS, g_{ID} = 5.0 nS, g_{IS} = 30.0 nS, g_{IP} = 7.0 nS, g_{SP} = 40.0 nS, $g_{DP(A)}$ = 10.0 nS, $g_{DP(B)}$ = 0.8 nS.

Inputs

For each B cell, the mean firing rate was fixed at a constant 10 Hz throughout the simulation. The firing rate of I cells varied with the stimulus. For cells with preferred orientations θ and a stimulus with orientation θ$_S$, the firing rate of the cell was determined by a Gaussian curve centered on θ$_S$ with a width of 18°, baseline firing rate of 20 Hz and peak firing rate of 30 Hz:

$$f_\theta = e^{-\frac{(\theta - \theta_S)^2}{2\sigma_S^2}} \cdot f_p + f_0$$

with f_p = 10 Hz, f_0 = 20 Hz, and σ_S = 18°.

Simulation Environment and Global Parameters

All simulations were carried out using Cortical Network Simulator (Mutch et al. 2010) written in Matlab (The Mathworks) and C, running on a custom PC with 2 GeForce 8800 Ultra GPUs (EVGA). The time step for intracellular and synaptic computations was 10 μs, intercellular spike-based communication was performed with a time step of 100 μs.

Results

Subtype-Specific Reduction of Interneurons in Dlx1$^{-/-}$ Visual Cortex

We first examined whether there is subtype-specific loss of interneurons in the adult visual cortex of *Dlx1$^{-/-}$* mice, as reported in the somatosensory cortex of these mice (Cobos et al. 2005). Immunohistochemistry on the visual cortex of adult *Dlx1$^{-/-}$* mice showed a reduction in calretinin+ (27.7 ± 2.7%, $P < 0.05$), NPY+ (30.2 ± 1.3%, $P < 0.01$), somatostatin+ (16.1 ± 7.0%, $P < 0.05$) neurons compared with wild types (Fig. 1*A–G*). The total number of parvalbumin+ interneurons was unchanged in the mutant mice (Fig. 1*G*). These data are similar to those previously described in other cortex of *Dlx1$^{-/-}$* mice (Cobos et al. 2005). Furthermore, analysis by cortical laminae in the visual cortices of mutant mice and their control littermates revealed that the reduction in calretinin+, NPY+, and somatostatin+ neurons occurred predominately in layers 2-4 (Fig. 1*G*). Interestingly, while the total number of parvalbumin+ neurons appeared unchanged in the *Dlx1$^{-/-}$* visual cortex, there was an increase of parvalbumin+ neurons in layers 2/3 (27.6 ± 3.5%, $P < 0.05$). Thus, we identified a subtype-specific reduction of interneurons, particularly in the superficial layers, in the visual cortex of *Dlx1* mutant mice.

Normal Thalamic Function in Dlx1$^{-/-}$ Mice

Input to the visual cortex from the retina is first processed by the dLGN of the thalamus (Sherman and Spear 1982; Sherman

and Koch 1986). In addition, information processed in the dLGN is modulated by inhibitory input from the visual sector of the adjacent thalamic nRT and possibly by dLGN local circuit interneurons (Soltesz and Crunelli 1992). As *Dlx1* is expressed in the inhibitory neurons of the nRT (and its anlage, the ventral thalamus) and is not expressed in the dLGN (Bulfone et al. 1993; Jones and Rubenstein 2004), we assessed whether there is loss of GABAergic neurons in both the nRT and the dLGN of adult *Dlx1$^{-/-}$* mice. The number of *Gad67*+ cells in these regions appeared normal in *Dlx1* mutant mice (Fig. 2A,B). We also examined the membrane and synaptic properties of nRT and dLGN neurons in *Dlx1* mutants. We found no significant differences in these properties between *Dlx1$^{-/-}$* mice and their wild-type littermates at adult or juvenile ages (Table 1). In particular, no difference was detected in the frequency or

amplitude of sEPSCs recorded from nRT cells (Fig. 2C–F and Table 1). Similarly, we found no difference in the frequency or amplitude of sIPSCs recorded from dLGN relay neurons in *Dlx1$^{-/-}$* mice compared with wild-type littermates (Fig. 2G,H and Table 2). Based on these observations, we did not find any evidence for altered properties of the thalamic relay to visual cortex in the *Dlx1* mutant mice.

Intact Map Organization and Ocular Dominance in *Dlx1$^{-/-}$* Mice

Given the reduction in dendrite-targeting cortical interneurons in *Dlx1$^{-/-}$* mice, we next asked whether the overall organization of thalamocortical inputs to visual cortex is altered in these mice. We carried out intrinsic signal optical imaging in V1 of *Dlx1$^{-/-}$* mice and their wild-type littermates and
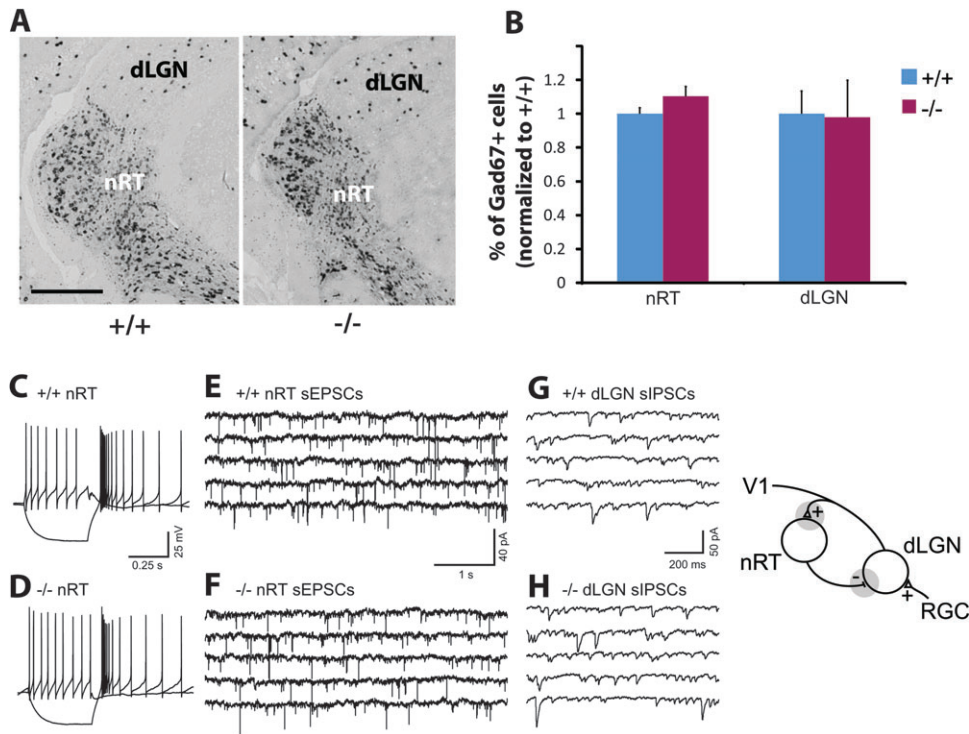

Figure 2. Adult *Dlx1$^{-/-}$* mice showed normal thalamic synaptic function. (*A*) Examples of representative *Gad67*+ cells, as shown by in situ hybridization, in the nRT and dLGN of the thalamus from *Dlx1$^{+/+}$* and *Dlx1$^{-/-}$* littermates. Scale bar: 250 μm. (*B*) The percents of *Gad67*+ cells in nRT and dLGN in the thalamus of *Dlx1$^{-/-}$* mice (*n* = 4), normalized to that in *Dlx1$^{+/+}$* littermates (*n* = 5), were quantified (*P* > 0.05 for both comparisons). (*C,D*) Representative current clamp recordings from individual cells in the nRT of wild-type (*C*) and *Dlx1$^{-/-}$* (*D*) mice. Both wild-type and *Dlx1$^{-/-}$* nRT cells responded to membrane hyperpolarizations with typical high frequency, long duration (>100 ms) rebound bursts of action potentials. The same nRT cells responded to depolarizing current steps with typical "tonic" firing mode with prominent fast spike after-hyperpolarizations evident. (*E,F*) Representative traces of whole-cell voltage clamp recordings of sEPSCs of individual neurons from nRT of wild-type (*E*) and *Dlx1$^{-/-}$* mice (*F*). Each trace contains 25 s of continuous recording with a holding potential of −85 mV when corrected for junction potential. (*G,H*) Representative traces of whole-cell voltage clamp recordings of sIPSCs of individual neurons from dLGN of wild-type (*G*) and *Dlx1$^{-/-}$* mice (*H*). Each trace contains 5 s of continuous recording with the membrane potential clamped at −64 mV. In schematic of the visual thalamic relay at right, gray circles represent the synaptic loci in the thalamic network that we studied.

Table 1

Passive, active, and synaptic properties of nRT cells in *Dlx1$^{+/+}$* and *Dlx1$^{-/-}$* mice

nRT	Passive membrane properties			Spontaneous excitatory postsynaptic currents				
	Capacitance (pF)	Input resistance (MΩ)	Membrane time constant (ms)	Frequency (Hz)	Amplitude (pA)	Rise time (ms)	Half-width (ms)	Decay time (ms)
+/+ (adult; 10)	40.3 + 5.8	330.2 + 27.7	37.0 + 5.9	4.6 + 0.7	−25.5 + 1.2	0.7 + 0.0	0.2 + 0.0	1.7 + 0.2
−/− (adult; 16)	40.9 + 4.8	230.5 + 34.4	31.8 + 4.0	5.0 + 0.6	−28.7 + 1.5	0.7 + 0.1	0.2 + 0.0	1.6 + 0.2
+/+ (juvenile; 12)	56.3 + 4.5	341.5 + 36.8	36.1 + 3.4	9.2 + 1.7	−23.3 + 1.2	0.3 + 0.0	0.7 + 0.0	1.7 + 0.1
−/− (juvenile; 19)	52.0 + 3.8	342.2 + 33.2	33.3 + 3.4	8.9 + 1.6	−23.0 + 1.1	0.3 + 0.0	0.8 + 0.0	1.9 + 0.1

Note: No differences were observed in cell size (capacitance), input resistance or time constant, or in measure of synaptic excitation (as assessed via analysis of sEPSCs). Numbers in the first column indicate number of cells.

examined the retinotopic map organization, scatter of these maps, and distribution of eye-specific inputs (ocular dominance). None of these 3 properties differed significantly between the 2 mouse groups (Fig. 3).

Broadened Orientation Tuning in V1 of $Dlx1^{-/-}$ Mice

Next, we focused our investigation on orientation selectivity in V1 of $Dlx1^{-/-}$ mice and their wild-type littermates using single-unit recordings. We recorded 95 single units from 16 $Dlx1^{+/+}$ mice and 122 single units from 10 $Dlx1^{-/-}$ mice. In order to ensure reliable data and to minimize contamination by artifacts, we chose a conservative strategy for data selection: We eliminated cells with extremely low visually evoked spike counts, which can introduce statistical bias or error. Moreover,

our results from laminar analysis of interneuron subtypes showed that reduction in dendrite-innervating interneurons are mostly restricted to the superficial layers in the visual cortices of mutant mice. Thus, we focused our analysis on units in layers 2 through 4; these included 62 of 95 units in $Dlx1^{+/+}$ mice and 91 of 122 units in $Dlx1^{-/-}$ mice. Of these units, 69.4% (43 of 62 units) in $Dlx1^{+/+}$ mice and 76.9% (70 of 91 units) in $Dlx1^{-/-}$ mice were responsive to visual stimuli. Among these visually responsive units, 61.4% (27 of 43 units) in $Dlx1^{+/+}$ mice and 62.9% (44 of 70 units) in $Dlx1^{-/-}$ mice had highly reliable evoked firing rates (≥ 1 Hz evoked firing rates, see Materials and Methods). All of the following analyses were performed on these cells.

We first examined whether temporal dynamics of visually evoked responses are affected in the $Dlx1^{-/-}$ visual cortex. PSTHs of $Dlx1^{-/-}$ units were distinct from those of $Dlx1^{+/+}$ units (Fig. 4A). The significantly different components of the $Dlx1^{-/-}$ PSTHs included lower baseline firing rates prior to visual stimulus onset (Fig. 4B), lower transient response (single peaks with large amplitudes) to the stimulus onset (Fig. 4C) but higher firing rates in the late response to the stimulus (Fig. 4D). Thus, even a partial removal of dendrite-innervating interneurons alters the amplitude and dynamics of baseline and stimulus-driven responses.

Table 2
Properties of sIPSCs in $Dlx1^{+/+}$ and $Dlx1^{-/-}$ mice.

dLGN	Spontaneous inhibitory postsynaptic currents				
	Frequency (Hz)	Amplitude (pA)	Rise time (ms)	Half-width (ms)	90% width (ms)
+/+ (adult; 7)	18.0 + 4.7	−24.64 + 2.0	1.9 + 0.1	11.9 + 1.5	24.2 + 3.3
−/− (adult; 6)	22.8 + 3.4	−20.6 + 0.6	2.3 + 0.1	13.0 + 1.7	24.5 + 3.7

Note: No differences were observed in frequency, amplitude, or kinetics of sIPSCs in dLGN relay neurons. Numbers in the first column indicate number of cells.
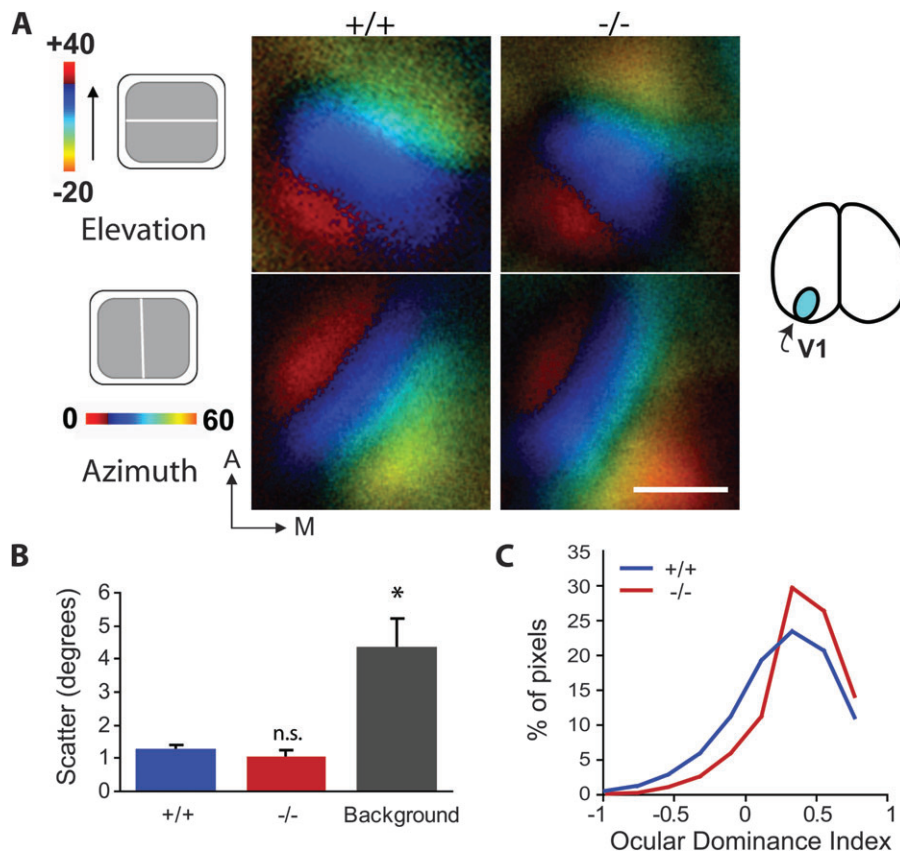

Figure 3. Adult $Dlx1^{-/-}$ mice showed normal retinotopic maps and binocular responses in V1. (A) Intrinsic signal optical imaging in V1 (from the same hemisphere across all animals, as indicated by the cyan area in the illustration at right) showed that $Dlx1^{-/-}$ mice have normal retinotopy in response to a drifting horizontal or vertical bar displayed to the contralateral eye. As examples, elevation and azimuth maps from a wild-type and $Dlx1^{-/-}$ littermate are displayed as a function of amplitude, normalized to the maximum pixel response in the field of view. Scale bar: 500 μm. (B) Average pixel scatter of retinotopic maps did not significantly differ between wild-type ($n = 3$) and $Dlx1^{-/-}$ ($n = 2$) mice. For comparison, scatter from nonvisual cortical regions was significantly higher than scatter in V1 of wild-type and $Dlx1^{-/-}$ mice ($P < 0.05$). (C) ODI pixel histograms from representative mice showed similar distributions in wild-type and $Dlx1^{-/-}$ binocular cortex. Average ODI values from V1 of $Dlx1^{-/-}$ versus wild-type mice (0.36 ± 0.08 vs. 0.30 ± 0.02) were not significantly different. For all panels, $*P < 0.05$.
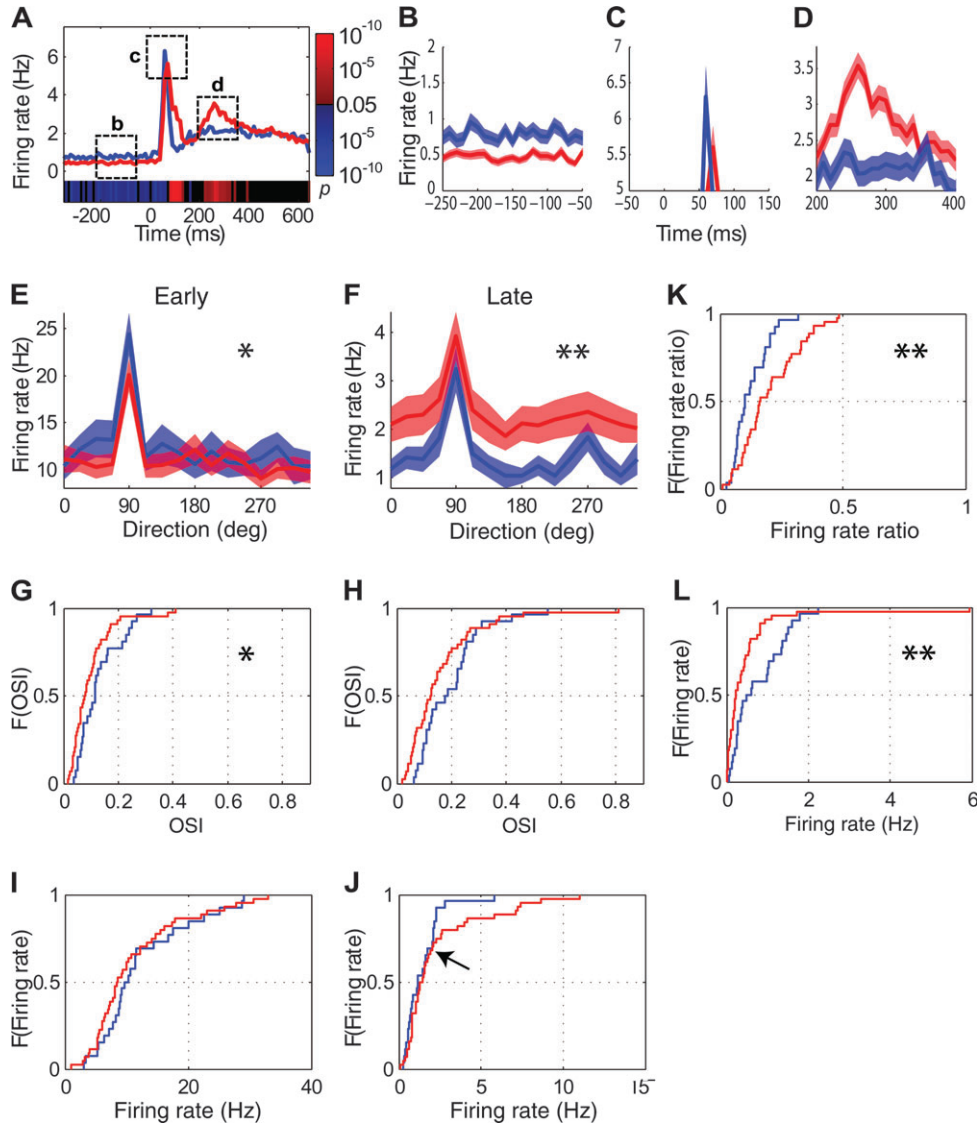
Figure 4. Orientation tuning and firing rates were affected in V1 of $Dlx1^{-/-}$ mice. (A) Average PSTH of $Dlx1^{-/-}$ cells (red line) was altered compared with the average PSTH from wild-type controls (blue line). Visual stimuli, with an onset at 0 ms, were presented for 2 s. Color bar at bottom of histogram shows running P values comparing the 2 histograms: blue bars denote $P < 0.05$ in instances where $Dlx1^{+/+}$ cells have higher firing rates than $Dlx1^{-/-}$ cells; red bars denote $P < 0.05$ in instances where $Dlx1^{+/+}$ cells have lower firing rates than $Dlx1^{-/-}$ cells; and black bars denote $P \geq 0.05$. Actual P values are shown on color bar at right. (B–D) Enlargements of the 3 time windows (indicated in panel A) demonstrate the changes in firing rates of $Dlx1^{-/-}$ cells. (E,F) $Dlx1^{-/-}$ cells showed altered average tuning curves based on early (E) and late responses (F). Here and in Figure 5, tuning curves spanning 360° are presented to illustrate different responses at 90° and 270°, both of which are at the preferred orientation but represent opposite directions. For panels B–F, the shaded areas represent mean ± SEM. (G,H) $Dlx1^{-/-}$ cells showed lower OSI values based on early (G) and late responses (H), as indicated by the cumulative density functions (CDFs) of OSIs. For Panels G–L (and similar panels in Figs 5 and 6), F on the y-axis represents CDF of OSI (G,H) or firing rates (I–L). (I,J) $Dlx1^{-/-}$ cells showed trends toward lower transient responses (I) and higher late responses (J) as indicated by the CDFs of firing rate. The arrow indicates a divergence point in the distribution (see text for details). (K) $Dlx1^{-/-}$ cells showed higher ratios of late to early responses. (L) $Dlx1^{-/-}$ cells showed lower spontaneous firing rates. For all panels except the color bars in panel A, blue lines depict $Dlx1^{+/+}$ cells; red lines depict $Dlx1^{-/-}$ cells. For all panels except panel A, *$P < 0.05$; **$P < 0.01$.

We next analyzed orientation tuning of V1 units in $Dlx1^{+/+}$ and $Dlx1^{-/-}$ mice. Based on our findings of altered response dynamics (described above), we separately analyzed orientation tuning for the early transient and late components of the visual response (for definition of early and late responses, see Materials and Methods). Tuning curves based on early transient response and late response were significantly different between $Dlx1^{+/+}$ and $Dlx1^{-/-}$ cells (Fig. 4E, early response: $P < 0.05$; Fig. 4F, late response: $P < 0.01$), likely due to differences in firing rates between the 2 curves. OSI values from the early response were significantly lower in the $Dlx1^{-/-}$ cells (Fig. 4G; $Dlx1^{+/+}$, 0.13 ± 0.02; $Dlx1^{-/-}$, 0.10 ± 0.01; $P <$

0.05). Similarly, OSIs from the late response in $Dlx1^{-/-}$ cells showed a trend toward lower values (Fig. 4H; $Dlx1^{+/+}$, 0.20 ± 0.02; $Dlx1^{-/-}$, 0.16 ± 0.02; $P = 0.06$). (Orientation tuning was less selective during the transient responses regardless of genotype. This likely reflects the contribution of an orientation-independent "onset transient" to these early responses. Tuning curves of late responses for individual cells from the top 20th percentile of OSI distributions in each of the $Dlx1^{+/+}$ and $Dlx1^{-/-}$ groups are shown in Supplementary Figs 1a and 1b, respectively). In sum, both early and late responses of V1 cells in $Dlx1^{-/-}$ mice are less orientation selective than cells in wild-type controls.

While the averaged evoked firing rates of the overall populations did not differ (Fig. 4*I*,*J*), there was a trend toward lower transient responses in $DlxI^{-/-}$ mice ($DlxI^{+/+}$, 12.38 ± 1.44 Hz; $DlxI^{-/-}$, 11.21 ± 1.15 Hz; $P > 0.05$) and higher late steady-state responses ($DlxI^{+/+}$, 1.44 ± 0.23 Hz; $DlxI^{-/-}$, 2.31 ± 0.37 Hz; $P > 0.05$). The ratios of late responses to early responses were significantly higher in $DlxI^{-/-}$ mice compared with $DlxI^{+/+}$ mice (Fig. 4*K*; $DlxI^{+/+}$, 0.12 ± 0.01; $DlxI^{-/-}$, 0.20 ± 0.02; $P < 0.05$). Comparisons of peak evoked firing rates revealed similar results to those of averaged evoked firing rates (Supplementary Fig. 2*A*,*B*). Spontaneous firing rates of $DlxI^{-/-}$ cells were significantly lower than those of $DlxI^{+/+}$ cells (Fig. 4*L*; $DlxI^{+/+}$, 0.77 ± 0.12 Hz; $DlxI^{-/-}$, 0.48 ± 0.14 Hz; $P < 0.05$).

Furthermore, while examining the evoked firing rates, we noticed a clear divergence in the distribution of evoked firing rate differences (based on late responses) between wild-type and $DlxI^{-/-}$ cells (Supplementary Fig. 3)—this divergence point was evident at the 30th percentile level of the distribution. Thus, approximately 30% of the cells (those with the highest evoked firing rates) seemed to be affected more severely than the rest of the population in the mutant mice. This breakpoint between the top 30% and bottom 70% of cells is consistent with the divergence point in the cumulative density function (CDF) in Figure 4*J* (indicated by an arrow).

We then examined in further detail the response properties of the 2 subgroups of cells in $DlxI^{-/-}$ mice and compared each with the equivalent fraction of cells in $DlxI^{+/+}$ mice. Interestingly, the top 30% and the bottom 70% of mutant cells showed drastically different changes in response properties (Fig. 5). For the top 30% of cells with the highest firing rates (Fig. 5*A*–*C*), it was the tuning curve based on late response that was more severely affected (early: $P < 0.05$; late: $P < 0.01$), whereas in the bottom 70% of cells (Fig. 5*D*–*F*), it was the tuning curve based on early response that was more affected (early: $P < 0.01$; late: $P > 0.05$). Spontaneous firing rates of the top 30% $DlxI^{-/-}$ cells were significantly lower than those of $DlxI^{+/+}$ cells (Fig. 5*G*; $DlxI^{+/+}$, 1.35 ± 0.20 Hz; $DlxI^{-/-}$, 0.91 ± 0.44 Hz; $P < 0.05$). The top 30% $DlxI^{-/-}$ cells showed a trend toward higher evoked early response (measured by average firing rates; for similar results from analysis of peak evoked firing rates, see Supplementary Fig. 2) than those of $DlxI^{+/+}$ cells (Fig. 5*H*; $DlxI^{+/+}$, 14.00 ± 3.29 Hz; $DlxI^{-/-}$, 16.19 ± 1.99 Hz; $P > 0.05$). As expected, the evoked late response of the top 30% $DlxI^{-/-}$ cells was significantly higher than that of $DlxI^{+/+}$ cells (Fig. 5*I*; $DlxI^{+/+}$, 2.18 ± 0.56 Hz; $DlxI^{-/-}$, 5.14 ± 0.84 Hz; $P < 0.05$). It is possible that some of our recorded cells are inhibitory neurons, but none of the putative fast-spiking cells identified based on their waveforms were in the top 30% population.

In comparison, spontaneous firing rates of the bottom 70% $DlxI^{-/-}$ cells were significantly lower than those of $DlxI^{+/+}$ cells (Fig. 5*J*; $DlxI^{+/+}$, 0.51 ± 0.11 Hz; $DlxI^{-/-}$, 0.29 ± 0.05 Hz; $P < 0.05$). These cells showed a trend toward lower evoked early response (Fig. 5*K*; $DlxI^{+/+}$, 11.66 ± 1.53 Hz; $DlxI^{-/-}$, 9.13 ± 1.23 Hz; $P = 0.07$) and lower late response (Fig. 5*L*; $DlxI^{+/+}$, 1.11 ± 0.17 Hz; $DlxI^{-/-}$, 1.12 ± 0.10 Hz; $P > 0.05$). We did not detect a significant difference between the OSIs of the top 30% $DlxI^{+/+}$ and $DlxI^{-/-}$ cells but did notice a trend toward lower OSIs in the bottom 70% $DlxI^{-/-}$ cells (Supplementary Fig. 4). Thus, lack of $DlxI$ results in changes in firing rates (especially during the late response) in the $DlxI^{-/-}$ mice, and these changes particularly affect a subpopulation of cells.

Furthermore, we performed similar analysis on responses of cells in layers 5–6; these included 20 of 33 units (60.6%, from 16 $DlxI^{+/+}$ mice) and 15 of 31 units (48.4%, from 10 $DlxI^{-/-}$ mice) that were responsive to visual stimuli. Among these visually responsive units, 10 of 20 units (50%) in $DlxI^{+/+}$ mice and 8 of 15 units (53.3%) in $DlxI^{-/-}$ mice had highly reliable evoked firing rates ($\geqslant$1 Hz evoked firing rates, see Materials and Methods). Interestingly, compared with units in layers 2–4 (Fig. 4*E*,*F* and Supplementary Fig. 5*A*,*B*), only the tuning curves based on early transient response of cells in layers 5–6 were significantly different between $DlxI^{+/+}$ and $DlxI^{-/-}$ mice (Supplementary Fig. 5*D*,*E*, early response: $P < 0.01$), where $DlxI^{-/-}$ units exhibited higher firing rates than $DlxI^{+/+}$ units at all orientations. This is consistent with our observation that in layers 5–6 of $DlxI^{-/-}$ mice, the numbers of calretinin+, NPY+, and somatostatin+ neurons are relatively unchanged (Fig. 1*G* and Supplementary Fig. 5*F*). In contrast, $DlxI^{-/-}$ cells in layers 2–4 showed higher late response levels than $DlxI^{+/+}$ units (Supplementary Fig. 5*A*,*B*), consistent with a reduction in calretinin+, NPY+, and somatostatin+ neurons and an increase in parvalbumin+ neurons in these layers (Fig. 1*G* and Supplementary Fig. 5*C*; see also Discussion). We did not detect significant differences in the other response properties, including OSI or evoked firing rates during early or late responses as well as spontaneous firing rates, between $DlxI^{+/+}$ and $DlxI^{-/-}$ units in layers 5–6 (data not shown).

Modeling the Contribution of Inhibitory Neuron Subtypes to Orientation Tuning

To further understand the changes in orientation selectivity and response level in $Dlx1$ mutant mice, we constructed a simple computational model that reproduced our experimental results. Specifically, we focused on building a model that captured the differential effects of the $DlxI^{-/-}$ interneuron loss on early and late responses, as characterized by their firing rates and OSI values. The model predicts the corresponding tuning properties of different interneuron subtypes and provides quantitative insight into potential mechanisms underlying reduced orientation selectivity in the $Dlx1$ mutant mice.

We based our model on a feed-forward architecture (Fig. 6*A*) that consisted of 3 cell types: excitatory pyramidal cells, STIs, and DTIs. Because the majority of the interneurons lost in the $DlxI^{-/-}$ cortex, namely somatostatin+, NPY+, and a fraction of calretinin+ cells, target dendrites of pyramidal cells, we did not explicitly include a fraction of calretinin+ cells that have been reported to target inhibitory neurons (Gonchar and Burkhalter 1999). All of these cells were modeled with Hodgkin–Huxley style dynamics, multiple compartments for pyramidal cells, and single compartments for inhibitory cells. All 3 cell types received both stimulus-driven and random background spike inputs. The 2 subtypes of interneurons provided inhibitory inputs onto the pyramidal cells. Each cell was assigned a preferred orientation and received input from presynaptic cells with similar orientation preferences. Comparable to the experimental data, one-third of the DTIs were silenced randomly in the $Dlx1$ mutant model.

We ran simulations using different combinations of input tuning for the STIs and DTIs and compared the results on firing rates and OSI values in mutant versus wild-type mice. We
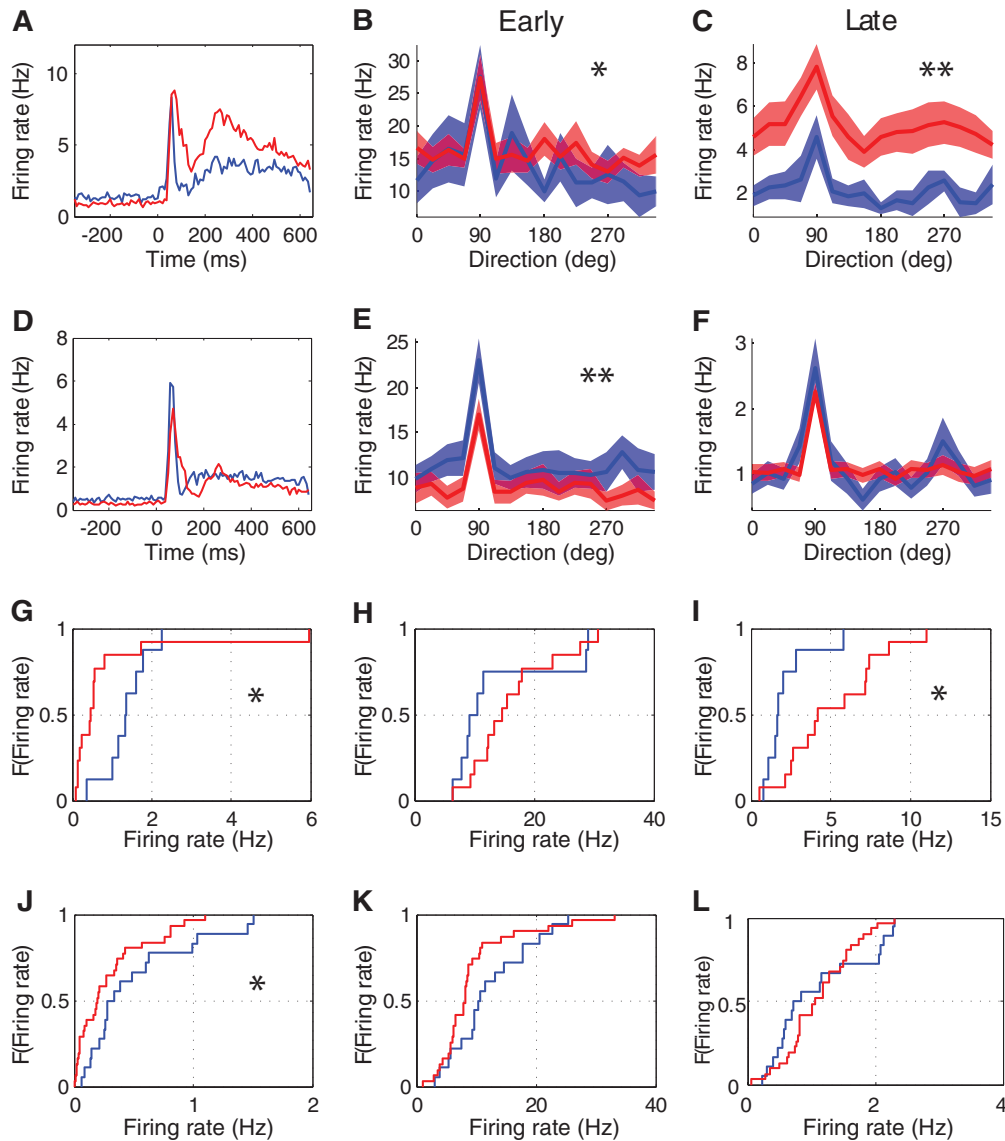
Figure 5. Orientation tuning and firing rates were affected differently between the top 30% of V1 cells with highest evoked firing rates and the rest (bottom 70%) of cells in *Dlx1*−/− mice, each compared with the equivalent fraction of cells in *Dlx1*+/+ mice. (*A*) Top 30% of *Dlx1*+/+ (*n* = 8) and *Dlx1*−/− (*n* = 13) cells showed very different average PSTHs. (*B,C*) For the top 30% of *Dlx1*−/− cells, the average tuning curve based on late responses (*B*) was more affected than that based on early responses (*C*). (*D*) Bottom 70% of *Dlx1*+/+ (*n* = 18) and *Dlx1*−/− (*n* = 31) cells showed similar average PSTHs. (*E,F*) For the bottom 70% of *Dlx1*−/− cells, the average tuning curve based on early responses (*E*) was more affected than that based on late responses (*F*). (*G*) Spontaneous firing rates of the top 30% *Dlx1*−/− cells were lower than those of *Dlx1*+/+ cells. (*H,I*) For the top 30% of *Dlx1*−/− cells, CDFs of average evoked firing rates showed a trend toward higher early responses (*H*) and significantly higher late responses (*I*) than those of *Dlx1*+/+ cells. (*J*) The bottom 70% *Dlx1*−/− cells showed a trend toward lower spontaneous firing rates. (*K,L*) For the bottom 70% of *Dlx1*−/− cells, CDFs of average evoked firing rates showed trends toward lower early responses (*K*) and lower late responses (*L*). For all panels, blue lines depict *Dlx1*+/+ cells; red lines depict *Dlx1*−/− cells. For all panels, *P < 0.05; **P < 0.01.

increased the impact of STIs onto pyramidal cells in the mutant model, based on the following rationale: 1) the number of parvalbumin+ cells was increased by 27.6 ± 5.48% in the superficial layers of *Dlx1*−/− visual cortex (Fig. 1*G*); 2) reduction in calretinin+ cells, some of which target GABAergic neurons in superficial layers (Gonchar and Burkhalter 1999), may result in decreased inhibition of inhibitory neurons, including STIs, in *Dlx1*−/− visual cortex; and 3) consistent with the above, spontaneous activity was lower in the *Dlx1* mutant cells (Fig. 4*L*). To account for an increase in the number of parvalbumin+ cells and possible homeostatic compensation in their synaptic inputs (see Discussion), we chose a 50% increase in STI impact. Among the different combinations, the only one that showed

reduced OSI values for both early and late responses in mutant mice, as indicated by our experimental data (Fig. 4*G,H*), contained STIs with narrower input tuning (with a maximum difference between presynaptic and postsynaptic preferred orientations of 30°, resulting in a mean OSI of 0.13) and DTIs with broader input tuning (with input tuning range of 90°, resulting in a mean OSI of 0.02) (Fig. 6*B,C*). Models with more sharply tuned dendrite-targeting inhibition led to changes in tuning that are less consistent with our experimental observations.

In addition, we also tested models with lower amounts of STI upregulation (e.g., 30% increased impact). These models replicated the increase in late response of mutant cells (this
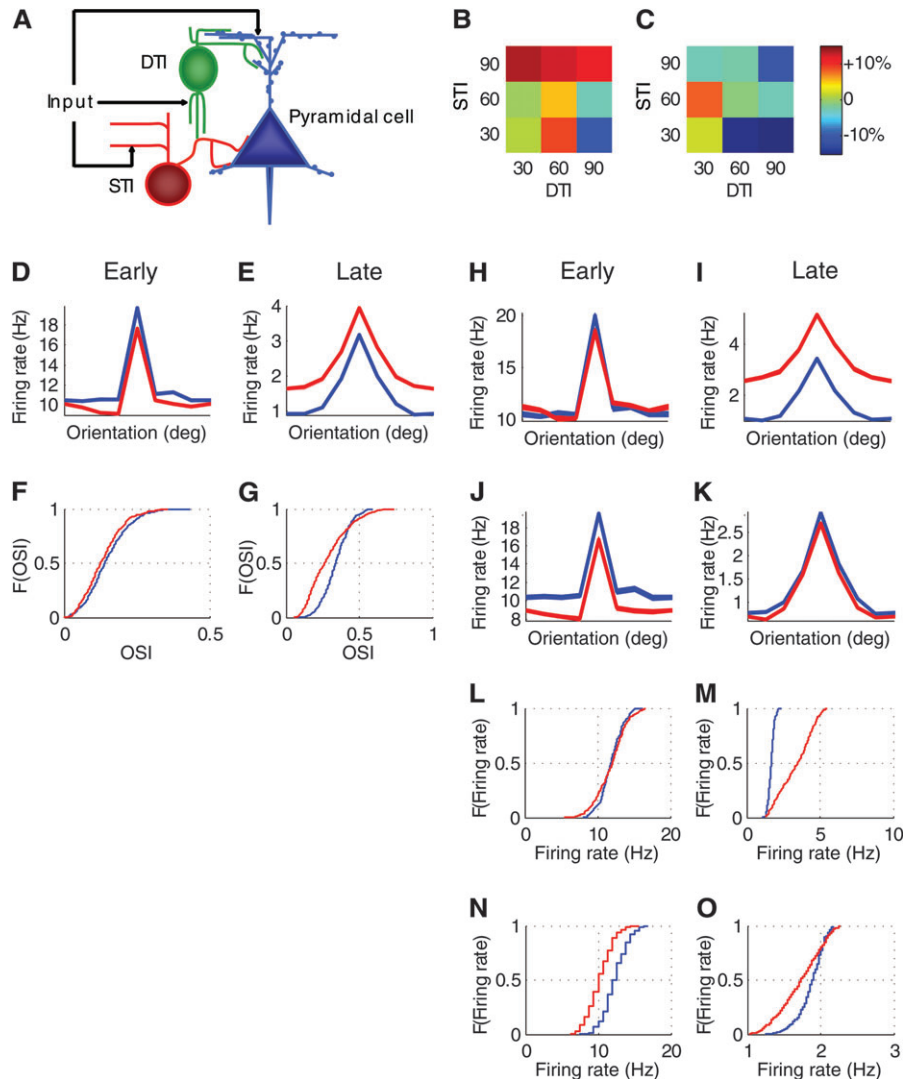
Figure 6. A network model, in which we varied the orientation tuning of DTIs and STIs, explains the key results in *Dlx1*^{−/−} mice and demonstrates the role of these interneuron subtypes in generating orientation selectivity and response levels of pyramidal neurons. (*A*) The basic architecture of our feed-forward model (see Materials and Methods). (*B,C*) After removing 33% of DTIs, changes in the OSI of pyramidal neurons during the early (*B*) and late responses (*C*) differed among 9 combinations of DTI and STI tuning properties. Numbers indicate ranges of differences (presented as ratios) between presynaptic and postsynaptic preferred orientations; the greater the number, the broader the tuning of the inhibitory neuron. Colors indicate directions (red: increase; blue: decrease; green: no change) and magnitudes (the darker the color, the greater the change) of changes in OSI. The only combination that produced lower OSI values during both early and late responses was the model with DTI = 90 and STI = 30 (both colors were blue). (*D–G*) In this best-fit model, tuning curves and CDFs for OSIs based on early (*D,E*) and late responses (*F,G*) showed similar changes to those in our experimental data (Fig. 4; see text for details). Tuning curves spanning 180° are presented because we did not include direction selectivity in our model. (*H–O*) The best-fit model displayed a divergence point of evoked firing rates at the 50th percentile. Changes in tuning curves (*H–K*) and CDFs for the firing rates (*L–O*) based on early (*H,J,L,N*) and late responses (*I,K,M,O*) of the top 50% of neurons (*H,I* and *L,M*) and the bottom 50% of neurons (*J,K* and *N,O*) were similar to those in our experimental results (Fig. 5; see text for details). For all panels in *D–O*, blue lines depict wild-type cells; red lines depict mutant cells (after silencing one-third of DTIs).

effect is robust and does not depend on the exact amount of STI upregulation, as long as DTIs are broadly tuned) but did not perform as well in replicating the changes in the spontaneous and early responses as the models with a 50% increase in STI impact.

In the best-fit model, tuning curves of the mutant cells showed changes that were highly consistent with our experimental results (compare Fig. 6*D-G* with Fig. 4*E-H*). In particular, the tuning curves based on late responses showed a major broadening and DC shift in the mutant model (Fig. 6*E*). OSI values calculated from early transient responses (*Dlx1*^{+/+}, 0.15 ± 0.003; *Dlx1*^{−/−}, 0.13 ± 0.003) and from late response (*Dlx1*^{+/+}, 0.34 ± 0.004; *Dlx1*^{−/−}, 0.29 ± 0.006) were both lower in the mutant cells (Fig. 6*F-G*). Similar to the experimental

data, the mutant cells showed lower early responses (*Dlx1*^{+/+}, 11.81 ± 0.07 Hz; *Dlx1*^{−/−}, 10.77 ± 0.10 Hz) and higher late responses (*Dlx1*^{+/+}, 1.52 ± 0.01 Hz; *Dlx1*^{−/−}, 2.29 ± 0.05 Hz).

Furthermore, both the best-fit model and the experimental data showed a divergence point between the wild-type and mutant distributions of their late response firing rates. In the model results, this divergence point was located at ~50th percentile of firing rates (the location of the divergence depends heavily on the exact connectivity between DTIs and pyramidal neurons). Since the absolute value is not important for our argument, we did not attempt to fit the model to reproduce the exact 30%/70% split as in our experimental data. Instead, we used the same method of splitting the population at the divergence point to compare the model results to the

experimental results). For the experimental data, we hypothesized that the 30% of $Dlx1^{-/-}$ cells with the highest late firing rates are cells that have lost most of their inputs from DTIs. We tested this hypothesis in the analysis of our model. We found that out of 512 cells, 264 (51.6%) did not lose any of their DTI inputs, whereas 197 (38.5%) lost at least 30% of their inputs. Over 90% (183/197) of these latter cells were in the top 50th percentile with the highest firing rates, thus supporting our hypothesis.

The model and experimental data were also in agreement with regard to changes in orientation selectivity and firing rates of these subpopulations of neurons (compare Fig. 6*H–K* with Fig. 5*B,C,E,F* and Fig. 6*L–O* with Fig. 5*H,I,K,L*). In the top 50% of cells with the highest firing rates, the tuning curves based on late responses were more severely affected (Fig. 6*H,I*), whereas in the bottom 50% of cells, the tuning curves based on early response were more affected (Fig. 6*J,K*). The top 50% mutant cells showed similar early responses to that of the control cells (Fig. 6*L*; $Dlx1^{+/+}$, 11.87 ± 0.10 Hz; $Dlx1^{-/-}$, 11.85 ± 0.13 Hz) but higher late responses (Fig. 6*M*; $Dlx1^{+/+}$, 1.67 ± 0.01 Hz; $Dlx1^{-/-}$, 3.36 ± 0.07 Hz). The bottom 50% $Dlx1^{-/-}$ cells exhibited lower early (Fig. 6*N*; $Dlx1^{+/+}$, 12.25 ± 0.11 Hz; $Dlx1^{-/-}$, 10.19 ± 0.11 Hz) and late responses (Fig. 6*O*; $Dlx1^{+/+}$, 1.87 ± 0.01 Hz; $Dlx1^{-/-}$, 1.72 ± 0.02 Hz).

Although the $Dlx1^{-/-}$ mouse represents a model with long-term loss of interneuron subtypes, we extended our modeling predictions to those from systems with acute silencing of one-third of the DTIs or STIs, in which the impact of STIs or DTIs, respectively, onto pyramidal cells remained unchanged (and therefore no homeostatic compensation was included). In these simulations, we used the combination of DTI and STI tuning properties in the best-fit model described above. Both manipulations resulted in increases in firing rates during early and late responses (Supplementary Fig. 6*A,B* and *D,E*). However, as shown by the ratios of late response firing rates to early response firing rates, while silencing STIs affected early and late responses to similar extents, silencing DTIs had a much stronger effect on late responses (Supplementary Fig. 6*C,F*). Furthermore, we observed this greater effect of DTI loss on late responses regardless of the tuning properties of DTIs and STIs: compared with an 8.8 ± 0.9% increase in the firing rate ratio after silencing STIs (averaged across all 9 combinations of DTI and STI tuning properties, as described above), silencing DTIs resulted in a 49.8 ± 1.6% average increase in this ratio (Supplementary Fig. 6*G*). Thus, DTIs may preferentially impact the sustained firing of target excitatory neurons, as suggested by our experimental data (Fig. 4*A*).

Discussion

We show that a subtype-specific reduction of dendrite-innervating interneurons in V1 leads to decreased orientation selectivity, lower spontaneous activity, and higher firing rates in late evoked responses. The effects on spontaneous and late evoked firing rates are more prominent in a subpopulation of neurons (~30%) with higher evoked firing rates than the remaining cells. Our computational model reproduces the experimental data and allows us to make predictions about possible tuning properties of DTI and STI interneuron subtypes. We suggest that the defects in V1 are due to intrinsic disruption of the visual cortical network, as no altered function of other components of the visual pathway was detected.

Role of Inhibition in Visual Receptive Field Properties

Inhibition has important functions in shaping ongoing and evoked cortical activity, and hence inhibitory interneurons have a key role in emergent properties of neuronal circuits (Mitchell et al. 2007; Chen et al. 2008). In the visual (and other sensory) cortex, inhibition appears to have a critical role in influencing the receptive field properties of neurons. The role of inhibition in shaping response features such as orientation selectivity (Ferster and Miller 2000) has been difficult to resolve unequivocally, due in part to multiple nonlinear properties (importantly, the spike threshold) available to cortical neurons for integrating inputs and generating selective responses (Priebe and Ferster 2008). Removal of inhibition leads to broadening of orientation and direction tuning (Sillito 1975; Sillito 1977; Jirmann et al. 2009), likely through mechanisms of network action (Somers et al. 1995). The tuning of inhibitory inputs to an individual neuron is variable (Vidyasagar et al. 1996; Anderson et al. 2000; Monier et al. 2003; Shapley et al. 2003) and depends at least partly on the location of neurons within relevant feature maps (Nelson et al. 1994; Schummers et al. 2002, 2007; Marino et al. 2005). Even less is known about the role of inhibition in the mouse visual cortex, which lacks orientation columns (Drager 1974; Antonini et al. 1999; Hubener 2003) and may therefore require additional inhibitory mechanisms such as higher synaptic specificity for sharpening orientation selectivity. Thus, inhibition likely plays diverse roles via specific synaptic connectivity from different cell types, in order to shape receptive field tuning properties of excitatory neurons. In this report, our data on $Dlx1^{-/-}$ mice provide evidence for a specific role of inhibition from subtypes of interneuron in producing sharp orientation tuning. Importantly, we found an increase in the firing rate of late responses in the mutant mice. This suggests that dendritic inhibition has temporally specific effects on neuronal responses to visual stimuli. Still, in the $Dlx1$ mutant mice, the impact of a 30% reduction of a subset of interneurons on cortical responses is modest, perhaps due to compensatory mechanisms (see below), the possibility that orientation selectivity may be generated prior to V1, and/or that a 30% reduction is not enough to cause a stronger effect.

Role of Interneuron Subtypes in Modulating Visual Responses

Orientation tuning of inhibitory interneurons in mouse visual cortex has been described as generally broader than that of noninhibitory neurons (Sohya et al. 2007; Niell and Stryker 2008; Liu et al. 2009; Kerlin et al. 2010). However, careful analysis of parvalbumin-expressing interneurons using targeted recordings from single marked cells demonstrates that they have a range of tuning properties, including very sharp orientation selectivity (Runyan et al. 2010). Intracellular recordings from cat V1 neurons also indicate diversity in electrophysiologically defined interneuron classes (Azouz et al. 1997). Thus, a subgroup of fast-spiking neurons, which are soma targeting, has been described as having broad orientation tuning (Nowak et al. 2008), although synaptic inputs to fast-spiking neurons in layer 4 are as narrowly tuned as those to regular-spiking neurons (Cardin et al. 2007). Clarifying properties and functional roles of interneuron subclasses will require more specific molecular-genetic markers, and refinement of technologies for selective removal of specific

subclasses (Luo et al. 2008). Our model predicts broader tuning for DTIs than for STIs, which is at least partly consistent with findings from soma-targeting parvalbumin-expressing interneurons (Runyan et al. 2010). We also show that DTIs may have a precise role in sharpening orientation selectivity of neurons in V1.

The different subclasses of interneurons likely modify pyramidal cell responses in functionally precise and distinct ways. Previous studies in the somatosensory cortex have characterized the synaptic dynamics of DTIs in vitro (Kapfer et al. 2007; Silberberg and Markram 2007) and the involvement of this interneuron subclass in gain modulation of a sensory response (Murayama et al. 2009), but the contribution of dendritic inhibition to feature-specific sensory information processing had remained unknown.

In visual cortical processing, DTIs may contribute specific inhibitory subfields to excitatory neuron receptive fields, whereas STIs may contribute broad complex-cell like inhibition (Hirsch et al. 2003; Lauritzen and Miller 2003; Palmer and Miller 2007). Our results suggest that the 2 major interneuron classes (DTIs and STIs) both sharpen orientation tuning, but the nature of their roles may be different, depending on their tuning properties and the location of their synapses. Based on predictions from our computational model, we postulate a possible mechanism that may account for our experimental data: STIs provide inhibitory input to the early response of the pyramidal neurons, are more narrowly tuned, and achieve sharpening of the early response by suppressing predominately the peak response to preferred orientations; DTIs provide inhibitory input to the late response, are more broadly tuned, and achieve sharpening of the late response by suppressing response to the preferred as well as nonpreferred orientations. In the mutant, a decrease in DTI inhibitory input leads to an overall (DC) increase in firing rates of the late responses, and hence a lower OSI calculated from the late response. Because input from STIs is increased, the peak response to preferred orientations will be selectively decreased relative to the responses to nonpreferred orientations, resulting in a lower OSI calculated from the early response.

Time Course of Responses

Our experimental observations and computational predictions provide convergent evidence that supports a model in which DTIs are critical for shaping the late responses of neurons to a stimulus: in layers 2–4 of *Dlx1* mutant mice, the most prominent phenotype is an increase in evoked late response of all cells, while the initial transient response is only moderately reduced. This can arise from 2 possible but not mutually exclusive mechanisms. First, the observation that the main effect is on late sustained responses could indicate that the early transient response is the result of the input and not affected by local processing, whereas sustained activity is the result of local (intralayer) computations and hence more sensitive to loss of interneurons. Second, this is consistent with the observation that fast-spiking parvalbumin+ STIs, which likely exert the initial inhibition of the evoked response, show a small increase in number in superficial layers of the mutant visual cortex, whereas the slower-spiking DTIs, which may be critical for suppressing the late response, are partially lost. Furthermore, in layers 5–6 where DTIs are unchanged (but STIs may be slightly increased), only the evoked early response is

increased. The distinct temporal effects of the 2 major interneuron subtypes are consistent with their intrinsic properties and synaptic connections. Fast-spiking parvalbumin+ STIs have membrane time constants that are comparable to or faster than pyramidal cells, while several subtypes of DTIs such as calretinin+ and somatostatin+ interneurons have longer membrane time constants (Beierlein et al. 2003; Ma et al. 2006; Cardin et al. 2007; Caputi et al. 2008). In contrast to the synapses onto or originating from parvalbumin+ cells, which are strongly depressing, synapses involving dendrites are often facilitating (Beierlein et al. 2003; Caputi et al. 2008). Furthermore, the location of synapses on the postsynaptic neuron supports a rapid action of STIs compared with a slower, delayed impact from DTIs.

Another line of support for these distinct temporal roles of interneuron subtypes arises from different postsynaptic GABAergic receptor types. GABA$_A$-mediated inhibition predominantly suppresses the early transient response, while GABA$_B$ receptors are involved in inhibition of the later sustained response (Pfleger and Bonds 1995; Allison et al. 1996). Several studies have suggested a differential distribution of GABA$_A$ and GABA$_B$ receptors in pyramidal neurons: GABA$_A$ receptors are localized both at the soma and in dendrites, while GABA$_B$ receptors may be restricted to dendrites (Newberry and Nicoll 1985; Connors et al. 1988; Kang et al. 1994). Moreover, GABA$_A$ and GABA$_B$ synapses may originate from distinct subpopulations of interneurons (Segal 1990; Otis and Mody 1992; Sugita et al. 1992; Benardo 1994), although a class of GABAergic interneurons, the neurogliaform cells, in contrast to other GABA-releasing cells, elicits combined GABA$_A$ and GABA$_B$ receptor–mediated responses (Tamas et al. 2003). Nonetheless, neurogliaform neurons express NPY (Karagiannis et al. 2009), which are among the reduced interneurons in the *Dlx1$^{-/-}$* cortex (Cobos et al. 2005). Together, these findings present possible mechanisms underlying our model, that slow dendritic GABA$_B$-mediated inhibition from DTIs (or a subclass thereof) is critical for the specific suppression of late evoked responses.

Furthermore, *Dlx1$^{-/-}$* neurons exhibit lower baseline firing rates (CA1 neurons in *Dlx1* mutants also exhibit reduced sEPSC amplitudes; D Jones, S Baraban, personal communication). We speculate that this decreased baseline activity may be attributable to a small increase in parvalbumin+ neurons in the superficial layers where most of the reduction in calretinin+, NPY+, and somatostatin+ neurons occurs and/or decreased disinhibition resulted from loss of the fraction of calretinin+ interneurons that innervate other interneurons in layer 2/3 of the cortex (Meskenaite 1997; Gonchar and Burkhalter 1999; Caputi et al. 2008). We found a distinct stratification in our data such that 30% of cells have higher firing rates and show much higher late responses, whereas the other 70% of cells have lower firing rates and are affected only in their early transient response. This result suggests that individual excitatory cells may have lost proportionally more, or less, DTI input, and as a result, may have experienced more, or less, homeostatic compensation from their remaining STI inputs. It is likely that one interneuron innervates multiple neurons, and one neuron receives inputs from multiple interneurons. Nevertheless, the similarity in the proportion of most affected cells (30%), and the proportion of DTI neurons lost (30%) in the mutant mice, suggests the possibility that the subset of lost DTI neurons had a specific target population of excitatory neurons, perhaps due to sparse distribution and small dendritic trees of these DTIs.

This hypothesis can be tested with future technical innovations, such as postnatal conditional mutagenesis of *Dlx1*, or strategies to selectively inactivate specific interneuron subtypes with optical-genetic tools.

Supplementary Material

Supplementary material can be found at: http://www.cercor.oxfordjournals.org/

Funding

Notes

References

Allison JD, Kabara JF, Snider RK, Casagrande VA, Bonds AB. 1996. GABAB-receptor-mediated inhibition reduces the orientation selectivity of the sustained response of striate cortical neurons in cats. Vis Neurosci. 13(3):559–566.

Anderson JS, Carandini M, Ferster D. 2000. Orientation tuning of input conductance, excitation, and inhibition in cat primary visual cortex. J Neurophysiol. 84(2):909–926.

Anderson SA, Eisenstat DD, Shi L, Rubenstein JL. 1997. Interneuron migration from basal forebrain to neocortex: dependence on Dlx genes. Science. 278(5337):474–476.

Antonini A, Fagiolini M, Stryker MP. 1999. Anatomical correlates of functional plasticity in mouse visual cortex. J Neurosci. 19(11): 4388–4406.

Ascoli GA, Alonso-Nanclares L, Anderson SA, Barrionuevo G, Benavides-Piccione R, Burkhalter A, Buzsaki G, Cauli B, Defelipe J, Fairen A, et al. 2008. Petilla terminology: nomenclature of features of GABAergic interneurons of the cerebral cortex. Nat Rev Neurosci. 9(7): 557–568.

Azouz R, Gray CM, Nowak LG, McCormick DA. 1997. Physiological properties of inhibitory interneurons in cat striate cortex. Cereb Cortex. 7(6):534–545.

Beierlein M, Gibson JR, Connors BW. 2003. Two dynamically distinct inhibitory networks in layer 4 of the neocortex. J Neurophysiol. 90(5):2987–3000.

Benardo LS. 1994. Separate activation of fast and slow inhibitory postsynaptic potentials in rat neocortex in vitro. J Physiol. 476(2):203–215.

Blatow M, Caputi A, Monyer H. 2005. Molecular diversity of neocortical GABAergic interneurones. J Physiol. 562(Pt 1):99–105.

Bulfone A, Puelles L, Porteus MH, Frohman MA, Martin GR, Rubenstein JL. 1993. Spatially restricted expression of Dlx-1, Dlx-2 (Tes-1), Gbx-2, and Wnt-3 in the embryonic day 12.5 mouse forebrain defines potential transverse and longitudinal segmental boundaries. J Neurosci. 13(7):3155–3172.

Butt SJ, Fuccillo M, Nery S, Noctor S, Kriegstein A, Corbin JG, Fishell G. 2005. The temporal and spatial origins of cortical interneurons predict their physiological subtype. Neuron. 48(4):591–604.

Butt SJ, Sousa VH, Fuccillo MV, Hjerling-Leffler J, Miyoshi G, Kimura S, Fishell G. 2008. The requirement of Nkx2-1 in the temporal specification of cortical interneuron subtypes. Neuron. 59(5):722–732.

Caputi A, Rozov A, Blatow M, Monyer H. 2008. Two calretinin-positive GABAergic cell types in layer 2/3 of the mouse neocortex provide different forms of inhibition. Cereb Cortex. 19(6):1345–1359.

Cardin JA, Carlen M, Meletis K, Knoblich U, Zhang F, Deisseroth K, Tsai LH, Moore CI. 2009. Driving fast-spiking cells induces gamma rhythm and controls sensory responses. Nature. 459(7247): 663–667.

Cardin JA, Palmer LA, Contreras D. 2007. Stimulus feature selectivity in excitatory and inhibitory neurons in primary visual cortex. J Neurosci. 27(39):10333–10344.

Chen Y, Martinez-Conde S, Macknik SL, Bereshpolova Y, Swadlow HA, Alonso JM. 2008. Task difficulty modulates the activity of specific neuronal populations in primary visual cortex. Nat Neurosci. 11(8):974–982.

Chow A, Erisir A, Farb C, Nadal MS, Ozaita A, Lau D, Welker E, Rudy B. 1999. K(+) channel expression distinguishes subpopulations of parvalbumin- and somatostatin-containing neocortical interneurons. J Neurosci. 19(21):9332–9345.

Chung S, Ferster D. 1998. Strength and orientation tuning of the thalamic input to simple cells revealed by electrically evoked cortical suppression. Neuron. 20(6):1177–1189.

Cobos I, Borello U, Rubenstein JL. 2007. Dlx transcription factors promote migration through repression of axon and dendrite growth. Neuron. 54(6):873–888.

Cobos I, Calcagnotto ME, Vilaythong AJ, Thwin MT, Noebels JL, Baraban SC, Rubenstein JL. 2005. Mice lacking Dlx1 show subtype-specific loss of interneurons, reduced inhibition and epilepsy. Nat Neurosci. 8(8):1059–1068.

Connors BW, Malenka RC, Silva LR. 1988. Two inhibitory postsynaptic potentials, and GABAA and GABAB receptor-mediated responses in neocortex of rat and cat. J Physiol. 406:443–468.

DeFelipe J. 1993. Neocortical neuronal diversity: chemical heterogeneity revealed by colocalization studies of classic neurotransmitters, neuropeptides, calcium-binding proteins, and cell surface molecules. Cereb Cortex. 3(4):273–289.

Destexhe A, Mainen ZF, Sejnowski TJ. 1994. Synthesis of models for excitable membranes, synaptic transmission and neuromodulation using a common kinetic formalism. J Comput Neurosci. 1(3):195–230.

Drager UC. 1974. Autoradiography of tritiated proline and fucose transported transneuronally from the eye to the visual cortex in pigmented and albino mice. Brain Res. 82(2):284–292.

Dragoi V, Sharma J, Sur M. 2000. Adaptation-induced plasticity of orientation tuning in adult visual cortex. Neuron. 28(1):287–298.

Eysel UT, Shevelev IA, Lazareva NA, Sharaev GA. 1998. Orientation tuning and receptive field structure in cat striate neurons during local blockade of intracortical inhibition. Neuroscience. 84(1):25–36.

Fagiolini M, Fritschy JM, Low K, Mohler H, Rudolph U, Hensch TK. 2004. Specific GABAA circuits for visual cortical plasticity. Science. 303(5664):1681–1683.

Ferster D, Chung S, Wheat H. 1996. Orientation selectivity of thalamic input to simple cells of cat visual cortex. Nature. 380(6571): 249–252.

Ferster D, Miller KD. 2000. Neural mechanisms of orientation selectivity in the visual cortex. Annu Rev Neurosci. 23:441–471.

Finn IM, Priebe NJ, Ferster D. 2007. The emergence of contrast-invariant orientation tuning in simple cells of cat visual cortex. Neuron. 54(1):137–152.

Galarreta M, Erdelyi F, Szabo G, Hestrin S. 2004. Electrical coupling among irregular-spiking GABAergic interneurons expressing cannabinoid receptors. J Neurosci. 24(44):9770–9778.

Golomb D, Amitai Y. 1997. Propagating neuronal discharges in neocortical slices: computational and experimental study. J Neurophysiol. 78(3):1199-1211.

Gonchar Y, Burkhalter A. 1999. Connectivity of GABAergic calretinin-immunoreactive neurons in rat primary visual cortex. Cereb Cortex. 9(7):683-696.

Gonchar Y, Wang Q, Burkhalter A. 2007. Multiple distinct subtypes of GABAergic neurons in mouse visual cortex identified by triple immunostaining. Front Neuroanat. 1:3.

Hirsch JA, Martinez LM, Pillai C, Alonso JM, Wang Q, Sommer FT. 2003. Functionally distinct inhibitory neurons at the first stage of visual cortical processing. Nat Neurosci. 6(12):1300-1308.

Hubener M. 2003. Mouse visual cortex. Curr Opin Neurobiol. 13(4):413-420.

Jirmann KU, Pernberg J, Eysel UT. 2009. Region-specificity of GABAA receptor mediated effects on orientation and direction selectivity in cat visual cortical area 18. Exp Brain Res. 192(3):369-378.

Jones EG, Rubenstein JL. 2004. Expression of regulatory genes during differentiation of thalamic nuclei in mouse and monkey. J Comp Neurol. 477(1):55-80.

Kang Y, Kaneko T, Ohishi H, Endo K, Araki T. 1994. Spatiotemporally differential inhibition of pyramidal cells in the cat motor cortex. J Neurophysiol. 71(1):280-293.

Kapfer C, Glickfeld LL, Atallah BV, Scanziani M. 2007. Supralinear increase of recurrent inhibition during sparse activity in the somatosensory cortex. Nat Neurosci. 10(6):743-753.

Karagiannis A, Gallopin T, David C, Battaglia D, Geoffroy H, Rossier J, Hillman EM, Staiger JF, Cauli B. 2009. Classification of NPY-expressing neocortical interneurons. J Neurosci. 29(11):3642-3659.

Kawaguchi Y, Kubota Y. 1997. GABAergic cell subtypes and their synaptic connections in rat frontal cortex. Cereb Cortex. 7(6):476-486.

Kawaguchi Y, Kubota Y. 1998. Neurochemical features and synaptic connections of large physiologically-identified GABAergic cells in the rat frontal cortex. Neuroscience. 85(3):677-701.

Kerlin AM, Andermann ML, Berezovskii VK, Reid RC. 2010. Broadly tuned response properties of diverse inhibitory neuron subtypes in mouse visual cortex. Neuron. 67(5):858-871.

Kubota Y, Kawaguchi Y. 1997. Two distinct subgroups of cholecysto-kinin-immunoreactive cortical interneurons. Brain Res. 752(1-2):175-183.

Lauritzen TZ, Miller KD. 2003. Different roles for simple-cell and complex-cell inhibition in V1. J Neurosci. 23(32):10201-10213.

Liodis P, Denaxa M, Grigoriou M, Akufo-Addo C, Yanagawa Y, Pachnis V. 2007. Lhx6 activity is required for the normal migration and specification of cortical interneuron subtypes. J Neurosci. 27(12):3078-3089.

Liu BH, Li P, Li YT, Sun YJ, Yanagawa Y, Obata K, Zhang LI, Tao HW. 2009. Visual receptive field structure of cortical inhibitory neurons revealed by two-photon imaging guided recording. J Neurosci. 29(34):10520-10532.

Luo L, Callaway EM, Svoboda K. 2008. Genetic dissection of neural circuits. Neuron. 57(5):634-660.

Ma Y, Hu H, Berrebi AS, Mathers PH, Agmon A. 2006. Distinct subtypes of somatostatin-containing neocortical interneurons revealed in transgenic mice. J Neurosci. 26(19):5069-5082.

Marin O, Rubenstein JL. 2001. A long, remarkable journey: tangential migration in the telencephalon. Nat Rev Neurosci. 2(11):780-790.

Marino J, Schummers J, Lyon DC, Schwabe L, Beck O, Wiesing P, Obermayer K, Sur M. 2005. Invariant computations in local cortical networks with balanced excitation and inhibition. Nat Neurosci. 8(2):194-201.

Markram H, Toledo-Rodriguez M, Wang Y, Gupta A, Silberberg G, Wu C. 2004. Interneurons of the neocortical inhibitory system. Nat Rev Neurosci. 5(10):793-807.

Meskenaite V. 1997. Calretinin-immunoreactive local circuit neurons in area 17 of the cynomolgus monkey, Macaca fascicularis. J Comp Neurol. 379(1):113-132.

Mitchell JF, Sundberg KA, Reynolds JH. 2007. Differential attention-dependent response modulation across cell classes in macaque visual area V4. Neuron. 55(1):131-141.

Monier C, Chavane F, Baudot P, Graham LJ, Fregnac Y. 2003. Orientation and direction selectivity of synaptic inputs in visual cortical neurons: a diversity of combinations produces spike tuning. Neuron. 37(4):663-680.

Murayama M, Perez-Garci E, Nevian T, Bock T, Senn W, Larkum ME. 2009. Dendritic encoding of sensory stimuli controlled by deep cortical interneurons. Nature. 457(7233):1137-1141.

Mutch J, Knoblich U, Poggio T. 2010. CNS: a GPU-based framework for simulating cortically-organized networks. Cambridge (MA): Massachusetts Institute of Technology MIT-CSAIL-TR-2010-013/CBCL-286.

Nelson S, Toth L, Sheth B, Sur M. 1994. Orientation selectivity of cortical neurons during intracellular blockade of inhibition. Science. 265(5173):774-777.

Newberry NR, Nicoll RA. 1985. Comparison of the action of baclofen with gamma-aminobutyric acid on rat hippocampal pyramidal cells in vitro. J Physiol. 360:161-185.

Niell CM, Stryker MP. 2008. Highly selective receptive fields in mouse visual cortex. J Neurosci. 28(30):7520-7536.

Nowak LG, Sanchez-Vives MV, McCormick DA. 2008. Lack of orientation and direction selectivity in a subgroup of fast-spiking inhibitory interneurons: cellular and synaptic mechanisms and comparison with other electrophysiological cell types. Cereb Cortex. 18(5):1058-1078.

Otis TS, Mody I. 1992. Differential activation of GABAA and GABAB receptors by spontaneously released transmitter. J Neurophysiol. 67(1):227-235.

Palmer SE, Miller KD. 2007. Effects of inhibitory gain and conductance fluctuations in a simple model for contrast-invariant orientation tuning in cat V1. J Neurophysiol. 98(1):63-78.

Palop JJ, Roberson ED, Cobos I. 2010. Step-by-step in situ hybridization method for localizing gene expression changes in the brain. Methods Mol Biol. 670:207-230.

Paxinos G, Franklin KBJ. 2001. The mouse brain in stereotaxic coordinates. San Diego (CA): Academic Press.

Pfleger B, Bonds AB. 1995. Dynamic differentiation of GABAA-sensitive influences on orientation selectivity of complex cells in the cat striate cortex. Exp Brain Res. 104(1):81-88.

Priebe NJ, Ferster D. 2008. Inhibition, spike threshold, and stimulus selectivity in primary visual cortex. Neuron. 57(4):482-497.

Qiu M, Bulfone A, Ghattas I, Meneses JJ, Christensen L, Sharpe PT, Presley R, Pedersen RA, Rubenstein JL. 1997. Role of the Dlx homeobox genes in proximodistal patterning of the branchial arches: mutations of Dlx-1, Dlx-2, and Dlx-1 and -2 alter morphogenesis of proximal skeletal and soft tissue structures derived from the first and second arches. Dev Biol. 185(2):165-184.

Racine RJ. 1972. Modification of seizure activity by electrical stimulation. II. Motor seizure. Electroencephalogr Clin Neurophysiol. 32(3):281-294.

Runyan CA, Schummers J, Van Wart A, Kuhlman SJ, Wilson NR, Huang ZJ, Sur M. 2010. Response features of parvalbumin-expressing interneurons suggest precise roles for subtypes of inhibition in visual cortex. Neuron. 67(5):847-857.

Schummers J, Cronin B, Wimmer K, Stimberg M, Martin R, Obermayer K, Koerding K, Sur M. 2007. Dynamics of orientation tuning in cat v1 neurons depend on location within layers and orientation maps. Front Neurosci. 1(1):145-159.

Schummers J, Marino J, Sur M. 2002. Synaptic integration by V1 neurons depends on location within the orientation map. Neuron. 36(5):969-978.

Segal M. 1990. A subset of local interneurons generate slow inhibitory postsynaptic potentials in hippocampal neurons. Brain Res. 511(1):163-164.

Shapley R, Hawken M, Ringach DL. 2003. Dynamics of orientation selectivity in the primary visual cortex and the importance of cortical inhibition. Neuron. 38(5):689-699.

Sherman SM, Koch C. 1986. The control of retinogeniculate transmission in the mammalian lateral geniculate nucleus. Exp Brain Res. 63(1):1-20.

Sherman SM, Spear PD. 1982. Organization of visual pathways in normal and visually deprived cats. Physiol Rev. 62(2):738-855.

Silberberg G, Markram H. 2007. Disynaptic inhibition between neocortical pyramidal cells mediated by Martinotti cells. Neuron. 53(5):735-746.

Sillito AM. 1975. The contribution of inhibitory mechanisms to the receptive field properties of neurones in the striate cortex of the cat. J Physiol. 250(2):305-329.

Sillito AM. 1977. The spatial extent of excitatory and inhibitory zones in the receptive field of superficial layer hypercomplex cells. J Physiol. 273(3):791-803.

Sohal VS, Zhang F, Yizhar O, Deisseroth K. 2009. Parvalbumin neurons and gamma rhythms enhance cortical circuit performance. Nature. 459(7247):698-702.

Sohya K, Kameyama K, Yanagawa Y, Obata K, Tsumoto T. 2007. GABAergic neurons are less selective to stimulus orientation than excitatory neurons in layer II/III of visual cortex, as revealed by in vivo functional Ca2+ imaging in transgenic mice. J Neurosci. 27(8):2145-2149.

Soltesz I, Crunelli V. 1992. GABAA and pre- and post-synaptic GABAB receptor-mediated responses in the lateral geniculate nucleus. Prog Brain Res. 90:151-169.

Somers DC, Nelson SB, Sur M. 1995. An emergent model of orientation selectivity in cat visual cortical simple cells. J Neurosci. 15(8):5448-5465.

Sugita S, Johnson SW, North RA. 1992. Synaptic inputs to GABAA and GABAB receptors originate from discrete afferent neurons. Neurosci Lett. 134(2):207-211.

Sussel L, Marin O, Kimura S, Rubenstein JL. 1999. Loss of Nkx2.1 homeobox gene function results in a ventral to dorsal molecular respecification within the basal telencephalon: evidence for a transformation of the pallidum into the striatum. Development. 126(15):3359-3370.

Swindale NV. 1998. Orientation tuning curves: empirical description and estimation of parameters. Biol Cybern. 78(1):45-56.

Tamas G, Lorincz A, Simon A, Szabadics J. 2003. Identified sources and targets of slow inhibition in the neocortex. Science. 299(5614):1902-1905.

Toledo-Rodriguez M, Blumenfeld B, Wu C, Luo J, Attali B, Goodman P, Markram H. 2004. Correlation maps allow neuronal electrical properties to be predicted from single-cell gene expression profiles in rat neocortex. Cereb Cortex. 14(12):1310-1327.

Varela JA, Sen K, Gibson J, Fost J, Abbott LF, Nelson SB. 1997. A quantitative description of short-term plasticity at excitatory synapses in layer 2/3 of rat primary visual cortex. J Neurosci. 17(20):7926-7940.

Vidyasagar TR, Pei X, Volgushev M. 1996. Multiple mechanisms underlying the orientation selectivity of visual cortical neurones. Trends Neurosci. 19(7):272-277.

Wang XJ, Buzsaki G. 1996. Gamma oscillation by synaptic inhibition in a hippocampal interneuronal network model. J Neurosci. 16(20):6402-6413.

Wang Y, Gupta A, Toledo-Rodriguez M, Wu CZ, Markram H. 2002. Anatomical, physiological, molecular and circuit properties of nest basket cells in the developing somatosensory cortex. Cereb Cortex. 12(4):395-410.

Wonders CP, Anderson SA. 2006. The origin and specification of cortical interneurons. Nat Rev Neurosci. 7(9):687-696.

Xu Q, Cobos I, De La Cruz E, Rubenstein JL, Anderson SA. 2004. Origins of cortical interneuron subtypes. J Neurosci. 24(11):2612-2622.

Xu X, Roby KD, Callaway EM. 2006. Mouse cortical inhibitory neuron type that coexpresses somatostatin and calretinin. J Comp Neurol. 499(1):144-160.

Yazaki-Sugiyama Y, Kang S, Cateau H, Fukai T, Hensch TK. 2009. Bidirectional plasticity in fast-spiking GABA circuits by visual experience. Nature. 462(7270):218-221.

Zhao Y, Flandin P, Long JE, Cuesta MD, Westphal H, Rubenstein JL. 2008. Distinct molecular pathways for development of telencephalic interneuron subtypes revealed through analysis of Lhx6 mutants. J Comp Neurol. 510(1):79-99.